DOI:
10.1016/j.aeolia.2018.07.001

Document Version
Peer reviewed version

Large-Scale Particle Image Velocimetry (LSPIV) of aeolian sand transport patterns

Andreas C.W. Baas[1] & Fabien van den Berg

[1] Department of Geography, King's College London, Strand, London WC2R 2LS, UK; andreas.baas@kcl.ac.uk (corresponding author).

Abstract

This paper presents results of laboratory testing and proof-of-concept field deployment of large-scale particle image velocimetry (LSPIV) using a consumer-level digital video camera to measure advection velocities of streamers and sand transport patterns over a beach surface. The LSPIV algorithm developed in this study employs interrogation windows of ten different sizes to resolve the displacement vector field at a range of scales. Laboratory testing shows that the vertical downward velocities and accelerations of falling batches of sand measured with the LSPIV method agree very closely with the theoretically predicted fall velocities and accelerations. The field experiment was successful in recording the advection of streamers at a frequency of 25 Hz over a field of view of 1.3×1.6 m^2 and over a period of 144 seconds. The vector field of streamer propagation could be resolved to a scale of 108 mm, exhibiting a mean advection speed of 4.01 m/s. Individual time-series segments however reveal that speeds fluctuate continuously between 3 and 7 m/s and with directional variability of 15-20°. Because of the experimental design these advection results may be representative of horizontal flight velocities of the saltating grains. 2D variograms and a time-space collage indicate length and time scale characteristics of streamers that are largely in line with previous studies. The high spatio-temporal variability of the measured advection and the lack of any link between local propagation speeds and grain cloud densities inside streamers confirm the importance of measuring boundary layer turbulence concurrently with the small-scale sand transport dynamics.

Keywords: streamers, advection speed, field experiment, Camber Sands

Running title: LSPIV of aeolian sand transport

1. Introduction

The past 15 years have seen an increasing interest in understanding small scale spatio-temporal variability in aeolian sand transport over beaches and desert surfaces in relation to turbulence structures or events in the near-surface boundary layer, in contrast to the traditional sand transport models that link bulk transport rates to a time-averaged shear velocity driving a uniform layer or blanket of saltating grains (Bauer *et al.*, 2013). Aeolian sand transport often occurs in the form of streamers: visually distinct, longitudinal slivers of wind-blown sand – also known as sand snakes – that move and meander downwind, and it is suggested that they originate with distinct eddies that impinge onto the sand surface and initiate transient saltation as they scrape across the bed (Baas, 2003; Baas & Sherman, 2005). The direct relationship between turbulence and sand transport has also been investigated along the concept of burst-sweep events (Wiggs & Weaver, 2012; Sterk *et al.*, 1998; Bauer *et al.*, 1998), and a number of recent studies have focussed on small-scale transport variability in relation to local surface controls such as surface moisture effects and thresholds (Davidson-Arnott & Bauer, 2009; Poortinga *et al.*, 2015), high-frequency 3D measurements of airflow and sediment transport (Walker *et al.*, 2009), sand transport in response to secondary airflow turbulence at reattachment points (Lynch *et al.*, 2013), and numerous field experiments testing and deploying small electronic sand transport sensors for high-resolution monitoring (Ellis *et al.*, 2009; Davidson-Arnott *et al.*, 2009; Hugenholtz & Barchyn, 2011; Schönfeldt, 2012; Udo, 2009; Bauer & Davidson-Arnott, 2014; Sherman *et al.*, 2011).

Further understanding of the links between aeolian sand transport and turbulence structures in the airflow requires more insight into the propagation speeds of streamers and pattern dynamics in the saltation field within a spatio-temporal framework (Baas, 2008). A first step toward a spatially explicit assessment of wind-blown sand has been the analysis of field imagery to obtain time-averaged streamer characteristics (Sherman et al., 2013). Now, techniques developed in Particle Image Velocimetry (PIV) and advances in digital imaging consumer products provide significant opportunities for comprehensive and high-resolution measurement of sand transport patterns and their temporal dynamics.

Standard PIV methods of various forms are typically restricted to small (cm) physical scales to measure the trajectory velocities of saltating sand particles as well as grain-scale processes such as impact, splash, rebound dynamics (Rice *et al.*, 1995,

1996; Wang *et al.*, 2008), and the Magnus effect (White & Schultz, 1977). Recent years have seen many wind tunnel studies of the saltation layer, measuring both horizontal and vertical saltation velocities at various stages of the flight trajectories as well as grain concentration profiles, using not only PIV, but also Laser-Doppler Velocimetry and Mie Scattering Diffusion techniques (among many others: Dong *et al.*, 2002, 2003, 2004; Kang *et al.*, 2008; Rasmussen & Sørenson, 2008; Yang *et al.*, 2007; Zhang *et al.*, 2007). Because of the delicate, elaborate, and expensive nature of industrial-grade PIV equipment nearly all saltation studies have been performed in laboratory wind tunnels, the only in-situ field experiment having been conducted by Greeley *et al.* (1996) using a high-speed (3000 frames-per-second) film camera on Pismo Beach, CA.

The PIV principle has in the last 15 years also been applied on a larger spatial scale in hydraulic investigations of water surface velocities along river reaches and movements of ice floes, in an application termed *Large-Scale* PIV (Muste *et al.,* 2008). This paper presents the results of a novel proof-of-concept deployment of LSPIV to measure the spatio-temporal dynamics of aeolian sand transport, the advection over the surface of whole clouds of saltating grains – streamers and patterns rather than individual particles.

2. Background: Large-Scale Particle Image Velocimetry

PIV is based on a Lagrangian approach of extracting displacement vectors of discreet objects (particles) by comparing their locations in two photographic images, separated by a small time period, within a fixed reference frame (Raffel *et al.*, 1998; Westerweel, 1997). PIV is traditionally used in fluid dynamics research in laboratory settings on a small (cm) scale, using flows seeded with neutrally buoyant particles (tracers), so that their trajectories are a close approximation of the fluid motions. A thin light sheet is projected to illuminate the tracers in a specific plane of the flow and streaming video or high-speed photography is used to acquire sequential images. The image processing technique to extract displacement vectors is a spatial cross-correlation analysis of 'interrogation windows' (small portions of the image showing tracers) between two frame captures, separated by a small time-difference, of the fixed field of view. A search algorithm determines the displacement of the window in the second frame relative to the first frame that maximizes the 2D cross-correlation. Combined with the known time-lapse the velocity vector for that location can be calculated, and this analysis is applied to a grid of interrogation windows to resolve the entire velocity vector field in

the viewing frame. In traditional PIV the image resolution needs to be sufficiently high to allow tracking of individual particles. This limits the physical scale of investigation and requires specialised illumination methods and imaging devices allowing high-speed acquisition, at rates on the order of 1000 fps (frames-per-second).

This basic PIV principle can also be applied to matching the displacement of portions of a continuous field pattern, rather than discrete particles, contained in the interrogation windows, and this *Large-Scale* PIV has been extensively developed by Ichiro Fujita and co-workers for the measurement of, for example, surface water velocities in river flow (Fujita *et al.*, 1998) and the motion of ice floes at river channel confluences (Ettema *et al.*, 1997). In these applications the spatial scale of investigation is much larger, filming river reaches on the order of 100s of metres in length from cameras positioned high above the banks, to resolve a velocity vector field at a horizontal resolution of meters (e.g. Bradley *et al.*, 2002; Lewis & Rhoads, 2015; Sutarto, 2015). A comprehensive review of the application of LSPIV in hydraulic research is provided by Muste *et al.* (2008).

In the study presented in this paper we apply LSPIV on an intermediate scale, filming sand transport patterns over a surface area on the order of metres and resolving a velocity field at a horizontal resolution of centimetres. For fluvial and marine research applications there are numerous computational LSPIV packages available, both commercial and freeware (e.g. Fudaa-LSPIV, RIVeR, PIVLab). These are optimised, however, for relatively slow-moving water flows and near-shore marine environments at relatively large spatial scales. Because of the novel application to much faster moving wind-blown sand and smaller scales here, we developed our own LSPIV algorithm, summarised in section 3, to allow full exploration of the parametrisation and scales of interrogation. The proof-of-concept study includes indoors lab testing – LSPIV of falling sand compared with predicted fall velocities – in section 4, followed by a pioneering field deployment (section 5) that has yielded credible and realistic results, described in section 6. Initial analysis of the data reveal interesting relationships within and between the transport patterns and advection speeds as a function of interrogation scales, that suggest some potentially useful implications concerning the boundary-layer turbulence that drives this wind-blown sand, and this is discussed in section 7.

3. Methods: Image Acquisition and LSPIV Algorithm

This study used a Canon XM2 PAL High Definition digital video camera, a standard consumer level product. The XM2 image acquisition device has three independent CCD arrays, one for each RGB colour (Red, Green, Blue), at a frame size of 576×720 pixels. The frames are captured at 25 fps (PAL norm) using a *progressive* scan, that is, the lines of each frame are stored in a single sequence. It is worth noting here that an *interlaced* scan pattern (a common standard setting) is not suitable, since it stores the odd lines of one frame interlaced with the even lines from the next. While this benefits smooth frame transitions and thus visual appearance of video imagery, it destroys the integrity of the image data in individual frames. The shutter time was fixed at $1/90^{th}$ of a second to ensure sharp contrast and minimize blurring of sand patterns. In both the lab and the field set-up the moving sand patterns were filmed from a distance of 2 to 3 metres, yielding an image resolution on the order of a few mm per pixel. The LSPIV algorithm, described below, was coded and run within the Matlab® environment on a Dell XPS laptop with a 2.5 GHz CPU.

Figure 1 illustrates the LSPIV algorithm and the associated terminology used in this study on a mock frame-pair, separated by a time interval Δt, showing the advection of a streamer moving toward the upper-left. The frames are acquired images of single-valued colour intensity of, for example, the Red colour component, showing contrast between the sand in motion and the background. In basic form, the algorithm matches up segments of the sideways-moving pattern visible in the frames to determine their displacement in the second frame compared to the first frame. A fundamental required assumption is that the temporal scale of dynamic changes of the pattern itself is much larger than the time-interval used to track its overall displacement, the so-called frozen-turbulence (or Taylor's) hypothesis, which has also formed the basis for the measurement of aeolian streamers (Baas & Sherman, 2005). Given that the characteristic time scale of response of the saltating sand grain population to wind fluctuations is on the order of a second (Butterfield 1998, Ma & Zheng 2011), the time-interval between video-frames of 0.04 seconds here is sufficiently small to consider the pattern to be effectively 'frozen' from one frame to the next while it is being advected.

In detail: an interrogation window of a certain size (referred to here as the 'source' window, S) is identified on the first frame, centred at pixel location (x, y). A search algorithm then evaluates all the possible interrogation windows (of the same size) within a defined searching area on the second frame ('destination' windows, D) at

horizontal and vertical displacements of Δx and Δy pixels relative to the position of S. The correspondence between the source and an individual destination window is calculated as the cross-correlation coefficient, r, of the pixel values or image intensity fields inside the interrogation windows, defined as:

$$r(\Delta x, \Delta y) = \frac{\sum_{ij}\left(IS_{ij} - \overline{IS}\right)\left(ID_{ij}(\Delta x, \Delta y) - \overline{ID}\right)}{\left[\sum_{ij}\left(IS_{ij} - \overline{IS}\right)^2 \sum_{ij}\left(ID_{ij}(\Delta x, \Delta y) - \overline{ID}\right)^2\right]^{1/2}} \quad (1)$$

where IS and ID represent colour Intensity in Source and Destination interrogation window respectively, overbars denote the areal mean and $i\,j$ refers to the pixels (rows and columns) in each interrogation window. Equation (1) may also be referred to as the mean-removed correlation, normalised by the joint variance. The algorithm calculates r for each possible destination window within the defined searching area and then determines which of these yields the maximum. The found optimal horizontal and vertical pixel displacements ($\Delta x_{r\text{-}max}$, $\Delta y_{r\text{-}max}$) are subsequently converted to velocity components, u and v, labelled to the location (x, y) on the first frame as:

$$\begin{aligned} u(x, y) &= R\,\Delta x_{r-\max} / \Delta t \\ v(x, y) &= R\,\Delta y_{r-\max} / \Delta t \end{aligned} \quad (2)$$

where R is the image resolution in m pixel^{-1}.

Depending on the size of the search area the procedure is computationally expensive, requiring, for example, 10,000 separate cross-correlation calculations for a search area of 100×100 pixels, which constitutes only 2.4% of the total area of a frame. Furthermore, in designing our application of LSPIV to monitor streamer movement the size of the interrogation window requires careful consideration: it needs to be effective for matching pattern displacement at a sufficiently local scale, but too small interrogation windows reduce or trivialize the maximum correlation leading to spurious and incongruous matching inside a large search area. The LSPIV search algorithm developed for this study explores this dilemma by evaluating the displacement vector field over a range of scale levels, using interrogation windows of 10 different sizes, and it uses the local displacements found at the larger scale to direct and constrain the search area for displacement vectors on the next scale down, in the manner of a telescoping

'zoom-in' procedure. In addition, the interrogation windows at each scale are tessellated across the frame with a 1/3 overlap (in each direction) to increase the resolution and coverage of the resolved vector field (x, y) locations. The dimensions of the interrogation windows preserve the 1:1¼ aspect ratio of the video frame size (576:720) to ensure equal coverage over the entirety of the frame (particularly relevant for the larger scale levels). The computational algorithm is further optimised by evaluating the (Δx, Δy) cross-correlations within a search area in two passes, first sub-sampling the area at a coarser resolution and then focussing on the region showing the highest correlations to resolve the cross-correlation 'peak' at the individual pixel scale.

Table 1 lists the relevant parameters for each scale level. Starting at a specified source window location (x, y) the algorithm establishes an initial 'guiding' displacement estimate derived from the resolved vectors at the previous (larger) scale level using an inverse-square-distance weighted interpolation. A rectangular search area is then established by extending a search radius in x and y direction around the initial estimate. The size of the resultant search area is thus equal to (radius×2 + 1) pixels on each side. The first pass sub-sampling is implemented at 'step-size' intervals within this area, and the second pass refines the exact location of the cross-correlation peak at pixel resolution within a 'step-size' radius around the sub-sample location with the highest first-pass correlation. Even with the optimised search algorithm, however, the processing is still computationally demanding: at scale level 8, for example, a single displacement vector estimation requires 146 cross-correlation calculations, and resolving the whole vector field requires nearly 170,000 calculations. PIV analysis of one frame-pair over all ten scale levels altogether involves over 1.4 million cross-correlation calculations, requiring roughly 40-50 seconds in the hardware & software environment used in this study. Particularly at the larger scales the matching of interrogation windows also requires specific treatment of frame edges contained within potential destination windows. In this study edges are handled by applying a suitable non-data masking template identically to both source and destination window, so that the cross-correlation calculation (equation 1) is purely restricted to valid i j pixels, thus reducing the effective correlation area used in resolving displacement vectors near the edge of the frame.

4. Lab testing

Prior to field deployment the overall feasibility and functioning of the LSPIV methodology was assessed in a laboratory experiment, filming sand falling from a known height at a predictable vertical velocity. Coarse sand with a uniform grain-size of 1.5 mm was strewn by hand from the top of a scaffold tower, at a release height of approximately 4.9 m above the base. Near ground level the sand was falling in front of a black background screen (to ensure good colour contrast) and filmed along a horizontal viewpoint (i.e. sand falling from top to bottom in the imagery) with the video camera mounted on a tripod at a height of approximately 1.30 m and a distance of roughly 2.75 m from the screen. The rate of manual release of sand at the top of the scaffolding was varied and laterally spread left and right to mimic in the vertical plane the meandering patterns observed in aeolian streamers over transport surfaces. This methodology thus simulated as closely as possible the anticipated plan-view (vertically downward) filming of horizontal sand transport patterns in the field. The screen background was flanked by vertical survey rods with centimetre markings visible in the view (see Figure 2a) to enable determination of pixel resolutions and image geometry. The camera imagery covered a field of view from 0.83 to 1.76 m above the ground at the focal plane of the falling sand, with a spatial resolution of approximately 1.62 mm per pixel. The descending sand had therefore accelerated from the release height over a fall distance of 3.14 m to the point where it entered the camera view at the top of the imagery, and traversing to a total fall distance of 4.07 m at the level where it exits the camera view at the bottom of the imagery. From this video imagery a sequence of 101 frames (4 seconds; see Supplementary Material Video 1) was selected as a good sample for determination of displacement vectors in the vertically downward falling sand patterns. The video sequences were stored and handled in AVI file format, which uses three 8-bit colour channels (RGB), each allowing intensity values ranging from 0 to 255. All the subsequent processing and analysis employs only the Red band of the imagery, as this displayed the most marked contrast between the sand and the black background screen.

4.1. Background separation

For the PIV methodology to function properly, the sand transport patterns in the video imagery need to be isolated from the visible background. Ambient light conditions, even in the laboratory setting, were still variable throughout the video-sequence, because the falling sheets of sand interact with the lighting angles to induce

reflections and shadows across broad areas of the background surface. Subtracting a 'clean' video-still (i.e. a frame where no sand was falling through the image) would thus introduce distortions of the sand pattern signal. Instead, for each frame about to be processed a 'static' background component is established by time-averaging pixel values over a moving window of 25 frames (equivalent to 1 second) centred around the analysis frame (i.e. from the 12 frames preceding to the 12 frames following). This time-averaged 'static' background is then subtracted from the specific frame image to extract the visual sand component, as illustrated in Figure 2b. For the video sequence of the laboratory experiment, the areal (across the image) mean background pixel intensity values ranges from a minimum of 84.1 to a maximum of 87.6 over the 4 seconds of film, with an overall mean of 85.7. The areal standard deviation of the background values ranges from 9.0 to 10.6 (proportional to the mean, i.e. as a Coefficient of Variability = σ/μ, it ranges from 10.6% to 12.1%), and the overall standard deviation over the 101 frames amounts to 9.7. This may be interpreted as a representative value of the background noise or underlying spatial variations as a consequence of ambient light changes in the imagery.

4.2. Results

The LSPIV analysis procedure was applied to the chain of 100 frame-pairs of the laboratory sequence, as illustrated in Figure 2. In the analysis procedures, as well as in the statistics of the background removal described above, the left-hand and right-hand parts of the imagery showing the survey rods and the rear of the scaffolding structure were stripped out and only the central 'working' section was analysed, covering an image area of 576 pixels in height by 444 pixels in width, equivalent to 0.933 × 0.719 m^2. At the pixel resolution of 1.62 mm the ten scale levels of rectangular search windows for displacement vector estimation translate to short-axis (height) scales of: [933, 622, 467, 311, 233, 156, 117, 78, 58, 39] mm, from largest to smallest. Figure 2c shows an example of displacement vector estimation from a frame-pair, frames 15 & 16 of the sequence, at scale levels 6 and 9 (156 and 58 mm respectively). The displacement vectors are overlain on the image of the source frame (#15) positioned from the centre of each interrogation window at their base, with a length scaling factor of 0.5, i.e. the vectors are drawn at half of their actual displacement distance relative to the pixel scale of the image.

While the LSPIV procedure determines displacement vectors for every available search-window node in the image at each scale level, the results require filtering to retain only vectors that are associated with parts of a moving sand pattern in the imagery. As the cross-correlation analysis of the LSPIV method is based on matching segments of these patterns, i.e. spatial variations, between interrogation windows, a resolved correlation is therefore only meaningful when the local patterning is stronger than the underlying spatial variability, i.e. the local variations at least exceed the general background noise. Applying the level of background noise determined in the previous section the results are therefore filtered to retain only displacement vectors associated with a standard deviation greater than 9.7 in their interrogation windows.

Histogram distributions of the cross-correlation coefficients of these qualifying displacement vectors, from all 100 frame-pair results collectively, are shown in Figure 3, for the different scale levels. The histograms show that the cross-correlations for the larger interrogation windows down to scale level 6 are particularly high, with their mean and mode between $r = 0.8$ and $r = 0.9$, and with the bulk of the distributions above $r = 0.5$. At smaller scales the distributions spread out toward a lower range of correlation coefficients with an accompanying shift of their mode, median, and mean, although even with the smallest interrogation window of 24×30 pixels more than half of the correlations are greater than 0.5. The distributions show smooth transitions from scale to scale and do not indicate a clear cut-off value or intrinsic correlation threshold for further filtering of displacement vectors. The analysis of LSPIV results that follows below is instead based throughout on weighted statistics and histograms, where the contributing displacement vectors are weighted proportional to their associated correlation coefficients.

Figure 4 presents (weighted) histograms of the vertical downward velocities in m s^{-1} at all interrogation scales, annotated with the weighted mean and standard deviation. Note that with the pixel resolution of 1.62 mm and the film rate of 25 frames-per-second a velocity of 1 m s^{-1} constitutes a displacement between a frame-pair of 25 pixels. Conversely, the maximum precision of velocity measurement is within 1 pixel per 0.04 s, which is here equivalent to 0.04 m s^{-1}. The histograms show relatively narrow distributions at the larger scales, with more significant tails of lower velocities introducing negative skew at smaller scales. The weighted mean velocity varies only slightly, decreasing from 4.7 m s^{-1} at the larger scales to a consistent velocity of 4.6 m s^{-1} at the smaller scales, with associated standard deviations that also remain consistent,

at 0.85 m s^{-1} (or 18% of the mean). A significant bulk of the distributions, however, indicates velocities well above 5 m s^{-1}.

For comparison the distributions of lateral velocity were also analysed (not shown). These displacement vectors indicate a tendency toward a negative horizontal velocity (i.e. toward the left-hand side of the image), ranging from a (weighted) mean of -0.09 m s^{-1} with a standard deviation of 0.15 at scale level 2, to a mean of -0.21 m s^{-1} with a standard deviation of 0.32 at level 10. The smallest interrogation scale includes a few instances of vectors with lateral speeds of up to 1.0 m s^{-1}.

Considering that the falling sand continues to accelerate during its descent through the PIV frame, average downward speeds were analysed for the top-half and bottom-half of the imagery separately. Figure 5 shows the (weighted) means with surrounding standard deviation error-bars across the scale levels, indicating that at the medium scale levels (4-6) the velocities in top-half and bottom-half are largely the same, but that at the smaller scales (8-10) the mean velocity in the bottom-half, at 4.68 m s^{-1} (σ: 0.70), is indeed greater than that in the top-half, 4.54 m s^{-1} (σ: 0.96), by about 0.14 m s^{-1} (although the difference is small relative to the standard deviations involved).

4.3. Evaluation

The LSPIV results may be compared with the theoretically predicted fall velocity of the sand grains at the respective fall depths. Over the descent distances in this laboratory experiment sand grains of 1.5 mm diameter have not yet reached their (constant) terminal fall velocity, and so the predicted downward velocities at specific fall depths – ranging here from 3.14 m at the top of the PIV imagery to 4.07 m at the bottom – are calculated by the methodology used previously in conjunction with the sand fall flume testing of Safires, as detailed in the appendix of Baas (2004). In brief, accelerations of 1.5 mm diameter spherical particles falling through still air are calculated using the Basset–Boussinesq–Oseen (B.B.O.) equation (Graf, 1971, p.31) and subsequently adjusted for natural sand grain shape according to an empirical correction determined for beach sand by Cui *et al.* (1983). Integration from point of release then yields a fall velocity as a function of time and distance. These calculations predict a fall velocity of 4.55 m s^{-1} at the centre of the PIV frame (1.30 m above the ground, or a fall depth of 3.61 m), velocities of 4.39 and 4.68 m s^{-1} at the heights of top entry and bottom exit, respectively, from the PIV frame, and velocities of 4.48 and 4.62 m s^{-1} at the centres of the top-half and bottom-half of the imagery, respectively.

The weighted mean downward velocities estimated from the LSPIV analysis correspond very closely with their respective semi-empirical predictions (to within 1% difference, barely exceeding the measurement precision in fact, see Table 2), though with a slight over-estimation that is more evident at the coarser interrogation scales, and with distributions that indicate a number of vector velocities well above the predictions. The differences may be attributable to errors in the LSPIV method and/or under-prediction of the true fall velocity of the grain populations in the experiment. With respect to the LSPIV analysis, the results of the measured *lateral* velocities include some obviously erroneous estimates of sideways speeds of up to 1 m s^{-1}. The mean lateral velocities show a consistent bias toward the left-hand side at all scale levels, however, which would be uncharacteristic of a random error in the method itself and could instead be explained by a real sideways motion imparted on the sand at release from the top of the scaffolding tower. This agrees with the practical observation that the main sand fall episodes appearing in the analysed footage occurred during the passage of sand release from right-hand side to left-hand side of the working section, i.e. along the negative horizontal velocity direction.

Instead of errors in analysis method, the minor differences between measured and predicted fall velocities, and in particular the relatively broad distributions of the former, may rather be due to (real) internal dynamics of and variations within the falling sand 'cloud' as it descends through the air. It may be considered that batches of sand (such as shown in Figure 2) fall through the air as a collective population which generates an associated downward draft of air with it. Thus the assumption of individual, solitary grains falling through still air that underlies the theoretical predictions of the B.B.O. equation does not hold properly, and the batch may be accelerating somewhat more quickly.

While an independent assessment of the potential error or the confidence estimates around the PIV analysis cannot be established directly from these lab tests, the method is performing in accordance with expectations, and its reliability and internal consistency is further supported by the measurements of acceleration from top half to bottom half in the imagery. At the coarser scale levels the acceleration is not distinguishable because the size of the interrogation windows is too large relative to the acceleration distance. At the smaller scale levels (8-10), however, the consistent acceleration by 0.14 m s^{-1} matches the theoretically predicted velocity change from the centre of the top-half to the centre of the bottom-half.

A comparison of histograms in Figure 4 and statistics as a function of scale-level, shown in Table 3, suggests that the distributions of measured velocities are highly similar from scale level 6 and upwards, which may imply that the resolved velocity field does not exhibit any internal dynamics at spatial scales smaller than that of level 6, which is 15.6 cm.

5. Field Experiment

The field deployment took place during the afternoon of 20 May 2006, at Camber Sands (50°56′00″N, 0°47′06″E) on the channel coast of SE England near Rye, on a broad dissipative beach with a low-amplitude ridge and runnel topography exposed at low tide. Wind conditions were not measured continuously, but a hand-held anemometer showed wind speeds fluctuating roughly between 8 and 10 m s^{-1} at a height of approximately 1.9 m above the ground, with an obliquely onshore direction. Aeolian sand transport was at any rate strong and persistent throughout the measurement period with numerous streamer patterns meandering and advecting across the beach surface, as is visible in Figure 6a. The video camera was mounted on a metal suspension framework and pointed vertically downward, with its lens at a height of approximately 2.0 m above the beach surface (Figure 6b). The heavy stainless steel H-frame was tightly secured with guy-wires and provided a stable platform, with no wind-driven shaking or vibrations observed. The black cardboard screen was placed horizontally flat on top of the sand surface in the camera's field of view, roughly parallel with the sand transport direction, and weighted down and flanked with survey rods on either side. The upwind border of the screen extended less than a metre beyond the right-hand side edge of the camera's field of view, which was slightly skewed relative to the alignment of the screen and survey rods (Figure 7a). A sand sample taken from the beach surface was analysed for sediment size distribution and shows a median grain size of 0.19 mm diameter, with 82% (by mass) of the sediment contained between diameters of 0.15 and 0.25 mm.

The pixel resolution of the video imagery was measured from the section of survey rod visible in the footage at 2.24 (± 0.03) mm/pixel, yielding a total field of view of 1.29 m in 'height' (spanwise to the dominant transport taking place from right to left in the imagery) and a 'width' (or streamwise distance) of 1.61 m. Based on the achieved pixel resolution, the maximum precision of velocity measurement is 2.24 mm per 0.04 s, equivalent to 0.056 m s^{-1}.

From the video imagery a sequence of 3600 frames was selected (frames #4500-8100 of a 11′35″ recording) as a representative sample of streamers advecting across the surface, and the LSPIV analysis was applied to these 144 seconds of data. In all the subsequent image processing and analysis the upper-right triangular area of the imagery showing the survey rod and sand deposited around it was masked out and excluded from vector displacement measurements.

Ambient light conditions varied continuously throughout the field experiment due to changing cloud cover and so background separation was achieved in the manner developed in lab testing (see previous section) using a moving averaging window of 25 frames (1 second). The areal (across the image) mean background pixel intensity values range from a minimum of 110.6 to a maximum of 122.3 over the 144 seconds of footage, with an overall mean of 114.1. The areal standard deviations of the background values range from 4.0 to 8.6 (CoVs of 3.5% and 7.1%), with an overall magnitude of 5.2 over the 3600 frames.

Figure 7 shows a worked example of the LSPIV analysis applied to a frame-pair (#7977-7978) of the selected footage, from the original RGB frames (Fig. 7a) to the sand signal extracted in the Red channel (Fig. 7b). The LSPIV results are shown as the displacement vectors overlain on the first frame of the pair for interrogation scales 4 and 8 (Fig. 7c), and the maps of associated correlation coefficients (Fig. 7d).

With the image resolution of 2.24 mm/pixel the ten scale levels of rectangular search windows for displacement vector estimation translate to short-axis (height) scales of: [1290, 860, 645, 430, 323, 215, 161, 108, 81, 54] mm, from largest to smallest. The supplementary material online includes original footage as well as video sequences of the displacement vectors overlain over the extracted sand signal.

6. Results

Interpreting the background standard deviation as a measure of the image noise, cross-correlation coefficients of the LSPIV results were filtered for vectors associated with standard deviations in their interrogation windows exceeding a value of 5.2. Figure 8 presents histogram distributions of these correlations at each scale level. The histograms show that the cross-correlations are significantly better than those achieved in the lab testing, with the bulk of correlations remaining above 0.8 for the 5 larger scales and above 0.6 for the five smaller scales. From scale level 6 onwards the distributions are particularly similar and consistent, with modes remaining at $r = 0.8$.

Scalar advection speeds in m s^{-1} are calculated from the image *x*-axis and *y*-axis components of the (filtered) displacement vectors, with the results shown in the weighted histograms of Figure 9. The distributions at the three lowest levels (1-3) are somewhat erratic, but at the higher scales the histograms are smooth and resemble the shape of a normal distribution, apart from heavy tails at the lowest speeds. The distributions indicate some speed estimates at unrealistically high speeds of up to 10 m s^{-1}. Weighted mean speeds decline slightly with scale level, ranging from 4.42 m s^{-1} at the coarsest interrogation scale to 4.03 m s^{-1} at the finest. The standard deviations increase from 1.13 m s^{-1} at level 1 upwards, peak at 1.74 m s^{-1} at level 5 and then decline to 1.53 m s^{-1} at the finest scale. The three highest scale levels (8-10) display particularly consistent means and standard deviations (Table 3). The worked example of Figure 7 shows how the LSPIV analysis on different interrogation scales reflect the displacement of the transport pattern in differing ways. On scale level 4, the size of the interrogation window (example shown in black) and the locations of the resolved vectors indicate how the algorithm tracks the displacement of larger patches of transport pattern that include multiple streamers or edges of streamers, with correlation coefficients relatively high and uniform over large parts of the frame. On scale level 8, in contrast, the size of the interrogation window and the resolved vector locations show how the algorithm tracks each streamer and transport patch individually. In particular, the map of correlation coefficients indicates that the tracking of the edges of a streamer is more reliable than tracking its centre-line. This is likely because contrasts and spatial variations that can be linked from one frame to the next are strongest for the edges of the transport patterns.

6.1. Time-series

The fluctuating wind-forcing during the experiment may be reflected in temporal changes in the advection of the streamer patterns. The LSPIV results were processed to determine speed and direction averaged per individual frame, compiled into a time-series of weighted means and standard deviation error-bars at a sampling period of 0.04 s. Figure 10 shows an overview of the mean advection speed time-series, resolved at scale level 5 (323 mm), for the entire 144 s period. It shows a strongly fluctuating and intermittent sequence, including various instances of measured speed dropping (close) to zero m s^{-1}. Two more informative, detailed views of the temporal dynamics of the pattern advection speed are shown in Figure 11, resolved at scale level 8 (108 mm).

The graphs include the direction of motion, expressed in compass degrees relative to the *x*-axis of the footage imagery (defined as zero degrees from right to the left), with positive angles indicating deflections to the right of the streamwise direction. The graphs furthermore show on the lowest axis the number of displacement vectors used in the statistics for each frame.

The two periods shown in Figure 11 display relatively continuous sequences with rising and falling advection speeds, and only occasional outliers. The time-series display advection speed varying largely between 3 to 7 m s^{-1}, with clear continuity from frame to frame (e.g. 36-40 s, 132-135 s). The internal variability of measured speeds within individual frames (indicated by the light-coloured error-bars around the mean time-series) is significantly smaller than the standard deviations reported for the whole 144 s dataset: during the first period, the average standard deviation is 0.85 m s^{-1}, and during the second period it is 0.76 m s^{-1} – compared with a standard deviation of 1.56 m s^{-1} for the whole 3600-frame distribution reported in Figure 9 and Table 3 (scale level 8). Conspicuous peaks and troughs in speed show connectivity between adjacent frames (e.g. time = ~61.5 s, ~135.5 s, ~142.5 s) and are not isolated outliers. It is noticeable that peaks in advection speed tend to be associated with relatively stable direction of motion (e.g. time = ~56.1 s, ~142.5 s), while troughs are associated with a rapid change in direction of motion accompanied with high directional variability within frames (e.g. time = ~44 s, ~135.5 s, ~143.3 s). The general direction of motion is somewhat different between the two periods, varying mostly between 15-30° in the first period (mean = 23.3°), and between 0-15° in the second period (mean = 8.5°). The direction of motion is particularly steady during period 133-139 s, with the exception at time = ~135.5 s, while the advection speed displays rising and falling trends. With regards to the number of vector measurements available per frame (N in Figure 11), the advection speed time-series appears more smooth and the direction of motion more steady when the number remains relatively high (e.g. 36-43 s, 132.5-135 s), while speeds fluctuate more erratically and directions are more variable when N is low (e.g. 43-50 s, 140-144 s).

6.2. No correlations with saltation density

Given the complex feedback of momentum exchange and dynamic drag between wind forcing and saltating grains, a dependency may exist between local densities of the saltation field in parts of streamers and their associated advection speeds. Using the magnitude of the sand signal (Red channel after background removal) as a proxy for

sand grain density, Figure 12 shows the advection speed of individual vectors versus the mean sand signal (pixel values) in their associated interrogation windows (averaged between source and destination window), at scale level 8, for the 28 s period shown in Figure 11a. We focus on this period as it is a continuous sequence of vector measurements with few outliers. The data include only vectors that exceed the threshold noise, and their associated correlation coefficient is indicated by the degree of blackness of the data point. The figure displays a great scatter cloud of points exhibiting no obvious relationship between density and speed. Non-linear curve-fitting of various functions (logarithmic, power, polynomial) reveals no statistically significant or meaningful dependencies. The thickest part of the cloud rests between sand densities of 1.5 to 7 and advections speeds of 2 to 6 m s^{-1}. A limiting trend is that very low advection speeds, below roughly 1.5 m s^{-1}, are restricted to relatively low mean sand densities of less than ~7. The other limiting trend of no points below a mean sand density of 1 is a consequence of the noise threshold, since the mean sand signal in the interrogation window scales with its standard deviation and very low signals are thus filtered out. Scatter plots similar to Figure 12 for the other scale levels all show the same characteristics and absence of any obvious relationship. Likewise, expanding the analysis to the entire 144 s sequence also displays a similar scatter cloud of points with no relationship.

While there may not be any correspondence between local saltation density and advection speed for small segments of streamers and transport patterns, the temporal fluctuations in frame-averaged speed, shown in the time-series of Figure 11, may still be presumed to relate to changes in wind-forcing in some way. Wind velocities were not measured directly during the field experiment, but instead the overall amount of saltating sand within the entire frame of the image may reflect on the overall relative wind forcing at any one time. Figure 13 presents a scatter plot of the mean advection speed per individual frame versus the image-wide mean sand signal present, again for the period shown in Figure 11a. Any clear dependency is absent in these scatter plots, however, mirroring the graph of Figure 12. The bulk of the frame-averaged advection speeds is distributed between 2 and 6 m s^{-1} irrespective of the overall amount of saltating sand in the full image frame.

6.3. Spatial coherence

Although not strictly an LSPIV application, the imagery of sand transport patterns was analysed for spatial coherence by calculating two-dimensional empirical variograms based on frames with active sand transport. A variogram reflects the average variance of a field variable at point-pairs as a function of their separation distance. A low variance represents a high spatial correlation. 2D variogram calculations are particularly intensive, so variograms were constructed for a 5-second sequence in the first period of Figure 11a (37-42 seconds) and for a 2-second sequence in the second period of Figure 11b (133-135 s). These two periods were selected for their visual presence of streamers as well as the relatively stable direction of movement. The core of the calculation used a routine developed by Schwanghart (2013) to determine a variogram for each frame in the sequence, using a random sample of 10,000 point-pairs per frame. The sampling is required to keep the computation manageable, since the total number of point-pair permutations per frame is of $O(10^{11})$. To ensure that only frames with sufficient sand transport patterning were used variogram data were only calculated for frames within the sequence where the mean sand intensity exceeded 1.5. For the 37-42 second sequence 94 frames qualified (out of 125), and for the 133-135 second sequence 35 frames out of 50 were used. The variogram data were then averaged over all frames in each sequence to produce the results shown in Figure 14. These show how the average variance as a function of separation distance rises very quickly in the spanwise direction to reach a plateau (the 'sill') at a range of approximately 75 pixels, equivalent to 17 cm, for both of the analysed periods. In the streamwise direction, however, the variance increases much more slowly and steadily and does not reach its 'sill' within the data range. The 2D patterns in the variograms conform to the LSPIV measured directions of movement during these periods. For the first period the angle of the low-variance 'trough' is 20 degrees from normal, which is similar to the average advection direction during this 5-second period in Figure 11a. For the second period the trough runs almost exactly frame-horizontal, close to the advection direction of approximately 5 degrees during these two seconds (Figure 11b).

6.4. Spatio-temporal continuity

The continuity of transport patterns over a longer sequence of frames (and thus time) is illustrated in the collage of Figure 15. This collage includes 51 frames covering 2 seconds near the start of the first period shown in Figure 11a, from 38-40s. Tiling starts from top-left (the first frame) with consecutive frames overlapped using the

displacement vector (in the reverse direction) determined at the scale of the whole frame (level 1), i.e. added consecutively to the lower-right as time progresses. Using Taylor's "frozen turbulence" hypothesis the resulting collage may be interpreted as a transport pattern map that has advected past the video-camera (moving toward the upper-left). Because of the oblique advection direction during this period the overlapping of frames can be seen in the saw-tooth edgings of the strip. The increase in obliqueness during the latter part of this 2-second sequence, between 39-40s in Figure 11a, is reflected in the strip curving toward a steeper incline in the lower-right. The axes reflect spatial distances based on the image resolution of 2.24 mm/pixel.

The collage shows a good continuity of individual streamers over many frames, as well as patterns that may perhaps be interpreted as Y-junctions: two 'mergers' in the first 2 metres, and one 'split' at $(x, y) \approx (5.5, 2.8)$. The lengths of identifiable streamer segments appear to be largely between 1 to 2 metres, while the potentially 'splitting' streamer in the middle of the strip covers a distance of roughly 3.5 metres. The edges between individual frames are visible in the collaging of streamers, i.e. the overlapping is not a perfect fitting, but this may be partly due to the fact that the collaging is based on whole-frame displacements, whereas individual streamers may be advecting at differing speeds and directions (*cf* the range of speeds and directions indicated with error bars around the curves in Figure 11a). Streamer widths are consistently on the order of 20 centimetres throughout the map.

7. Discussion

The main goal of the laboratory testing and field experiment reported here is to establish the feasibility of applying LSPIV to aeolian sand transport patterns, using standard consumer-level video camera equipment. The absence of collocated time-series measurements of wind speed is a significant limitation to this field experiment, and the LSPIV analysis presented here is therefore an exploration of the various lines of inquiry that are possible on the sand transport velocimetry data alone, as examples of the potential and scope of this method. The results may have some implications for understanding aeolian sand transport dynamics, although wider interpretation is restricted by the fact that a black cardboard surface was used.

7.1. Streamer characteristics

Before discussing the LSPIV results in detail, we compare the spatio-temporal characteristics of the transport patterns observed in the footage from Camber Sands with measurements of streamers at Windy Point, CA (Baas, 2003; Baas & Sherman, 2005), as well as the video-imagery analysis of streamers recorded at Jericoacoara, Brasil (Sherman *et al.*, 2013). Visual analysis of LSPIV videos (available in the Supplementary Material) shows streamers passing through with spanwise widths between 0.1 and 0.15 m, which compares well with the 0.1-0.2 m width derived from the Safire array at Windy Point. This general width is further confirmed by the 2D variogram results indicating that spanwise spatial correlation drops off beyond a scale of 17 centimetres. The footage further shows usually only one or two streamers in the frame at any one time, as in the example of Figure 7. Since the field of view covers a transverse span of 1 m on average (taking into account the masked area of the top-right), the lateral streamer density is only a little higher than that of 0.9 streamers m^{-1} reported at Windy Point, and similar to the average lateral spacing of 0.6-1.0 m for the streamers observed at Jericoacoara.

The duration of passage, or at-a-point life-time, of streamers in the LSPIV imagery is short: visual assessment suggests that it usually takes only 5 to 10 frames for a single streamer to pass through, and there are several instances where an individual streamer is visible in its entirety from head to tail within the 1.6 m 'long' frame. A mean advection speed of 4 m s^{-1} (Table 3) over durations of 5 to 10 frames (0.2 - 0.4 s) indeed yields streamwise lengths of 0.8 to 1.6 m. The short life-time of streamers conforms to the streamer time-scale of < 1 s inferred from spectral analysis of Windy Point data (Baas, 2006). The spatio-temporal map of Figure 15 likewise displays streamer segments of 1 to 2 metres in length. This map however also reveals potentially longer conjoined linear structures with Y-junctions, that may be interpreted as continuing streamers, and which reach lengths of 2 to 3.5 metres. This is though an order of magnitude smaller than the length-scales reported at Jericoacoara, where continuous transport pathways were identified at 10s of metres in length. These differences highlight the significant contrast between spatial coverage and length of streamers as measured at a local spot, compared to the common visual impression of a dense blanket of long and interwoven streamers at a middle distance (e.g. Figure 6a).

7.2. Advection speeds

The LSPIV results indicate a wide range of advection speeds for the transport patterns at Camber Sands, varying mostly between 3 and 7 m s^{-1}. Considering this range and temporal evolution of fluctuations and the relatively small standard deviations involved, the variations in advection speed and direction likely reflect real streamer pattern behaviour, rather than measurement distortions or errors. The consistency of advection speed statistics at scale level 8 and above (Table 3), as well as the mapping of correlation coefficients to individual streamer segments (Figure 7) at this scale suggest that LSPIV at an interrogation scale of 108 mm is suitable, and matches well with the spanwise widths of streamers (section 7.1). The similarity in advection speed histograms at the highest three levels (Figure 6) furthermore suggests that the resolved velocity fields do not exhibit any internal dynamics at spatial scales smaller than that of level 8 (108 mm).

The time-series of Figure 11 reveal the high temporal variability of the advection speeds, exceeding the potential analysis error as well as the within-frame variation. Figure 7, meanwhile, shows a good example of instantaneous spatial variability, with the main streamer in the centre of the frame moving horizontally to the left (a direction of zero degrees), while the streamer in the bottom left-hand half of the frame is propagating more toward the upper-left (a direction of roughly + 15°) and at a slightly lower speed. These lines of evidence confirm that the advection speed is highly variable over space and time, at spatial scales of 0.1 m and at temporal scales of less than 0.1 s. The coincidences between rapid decelerations and high directional variability described in section 6.1 further suggest small-scale, locally driven, advection dynamics.

The overall weighted mean advection speed of 4.0 m s^{-1} at level 8 for the whole 144 second sequence at Camber Sands compares well with results from the Windy Point experiments (Baas, 2003), where the passage of saltation fluctuations was measured along a transport-parallel transect of six Safires at an average propagation speed of 3.6 m s^{-1}.

The correlation coefficients of the LSPIV analysis of the field experiment are high throughout all interrogation scales, with the vast bulk exceeding 0.6 even at the smallest scale and with medians consistently above 0.8, as well as showing a better performance as compared with the lab testing at the higher scales. These high cross-correlations are achieved in spite of the noise-threshold filtering of vectors, which selects for higher local standard deviations within the interrogation window and therefore minimizes

'artificial' inflation of correlation coefficients associated with very low variances in the calculation (eq. 1).

7.3. Interpretations

The implications of the measured advection speeds of aeolian transport patterns are constrained by the use of the cardboard surface over which the passing streamers were filmed. The change in underlying transport surface as streamers arrive from the natural beach onto the cardboard in the view of the camera has two key impacts. First, the cardboard provides a more efficient rebound surface for saltating grains as the absence of bed impact and splash conserves more kinetic energy, and as the smoothness of the surface likely allows shallower forward rebound angles conserving more horizontal momentum. This effect may be somewhat restricted by the fact that the cardboard extends less than a metre beyond the upwind edge of the camera's field of view – a distance similar to an average saltation jump length – and so the flight speeds of the saltating grains that make up the transport patterns may not yet deviate very much from those over the natural beach surface upwind of the test surface. Second, the cardboard decouples the active sediment in motion from its normal bed supply and exchange base. The advection of streamers observed in the LSPIV imagery therefore results purely from the collective horizontal propagation of the sand grains inside the forms and excludes the active entrainment of new sediment at the leading edge of surface-skimming eddies, as is envisaged in the streamer model over a normal sedimentary transport surface (Baas & Sherman, 2005).

From theoretical considerations of ballistic trajectories Nalpanis *et al.* (1993) predict horizontal velocities of saltating grains at the apex of their trajectory to reach half of the wind speed at that height above the bed. The vertical wind profile was not monitored in this study, but the manual wind speed measurements of 8 to 10 m s^{-1} at 1.9 m height, with an estimated roughness length, z_0, during active sand transport on the order of 1 mm, yields an estimated wind speed of 4.2 to 5.2 m s^{-1} at 5 cm height (shear velocities of 0.4 to 0.5 m s^{-1}), suggesting grain flight velocities of 2.1 to 2.6 m s^{-1}: significantly lower than the advection speeds measured here. This theoretical estimate is, however, comparable to the measurements obtained from high-speed photography in a field experiment at Pismo beach, CA, by Greeley *et al.* (1996), showing a speed distribution mostly between 1.5 and 3.0 m s^{-1}, for grains with a modal diameter of 0.23 mm and shear velocities ranging from 0.2 to 0.45 m s^{-1}.

Wind tunnel studies, on the other hand, generally report much higher flight velocities, many based on PIV or laser-doppler velocimetry. Dong *et al.* (2004) report minimum velocities of 4 to 6 m s^{-1} at heights of 1 to 5 cm above the bed, respectively, for 0.2-0.3 mm grains at their lowest free-stream velocity, for example. Yang *et al.* (2007) show modal speeds of 2 m s^{-1} at 0.5 cm above the bed and 6 m s^{-1} at 4 cm height, for 0.1-0.2 mm grains at a shear velocity of 0.54 m s^{-1}. Zhang *et al.* (2007) indicate speeds of 2 and 3.5 m s^{-1} at heights of 1 and 5 cm, respectively, for 0.1-0.2 mm beach sand and their lowest free-stream velocity. Kang *et al.* (2008) report much higher speeds, of 4 to 6 m s^{-1} at 1 to 5 cm height, respectively, for 0.17-0.3 mm sand at their lowest free-stream velocity. A laser-doppler study by Rasmussen & Sørensen (2008), finally, reports velocities of 2.2 m s^{-1} at 1 cm height to 4-5 m s^{-1} at 5 cm height (shear velocities of 0.38-0.56 m s^{-1}). It is clear that wind tunnel results vary widely, some of which may be comparable to the advection speeds measured in this study, others generally reporting lower grain velocities. Wind tunnel studies suffer from significant scale limitations relative to field conditions however (Farrell & Sherman, 2006), as they do not reproduce the full spectrum of boundary layer turbulence seen in the field, lacking particularly the top-down coherent flow structures thought responsible for streamer formation. The advection speeds measured in the field experiment reported here may thus perhaps be interpreted as more representative of horizontal flight velocities under natural wind conditions.

The absence of correlation between sand density (proxy) and advection speed may be interpreted on two scale levels. The lack of correlation at the local scale, as shown in Figure 12, suggests there is no simple correspondence between streamer intensity and the momentum extracted from coherent flow structures. The only way to resolve this conundrum is by high-resolution measurement of the airflow concurrently with the sand transport patterns. At the scale of the entire frame (Figure 13), the absence of correlation between the image-wide mean sand density (as a proxy for the overall flow forcing conditions) and the mean advection speed suggests that the sand transport process is dominated by small-scale, local dynamics with high spatio-temporal variability. These results are furthermore commensurate with the inelastic saltation collision model proposed by Namikas (2003, 2006), which predicts that increasing transport rates primarily result from increasing grain quantities in saltation, rather than from saltating grains attaining higher forward velocities.

7. Conclusions

This study has demonstrated the viability of applying Large-Scale Particle Image Velocimetry to investigate aeolian sand transport in the field using consumer level video equipment. Lab testing shows a close agreement between measured and predicted vertical fall velocities of grain populations dropped from a height and the LSPIV methodology is also capable of detecting the gravitational acceleration within the field of view. The results from the field experiment show displacement estimates with high cross-correlation coefficients at all interrogation scales and the observed advection speed statistics, their high spatial and temporal variability, and the characteristics of the transport patterns are consistent with our current understanding of streamer formation and behaviour and the associated spatio-temporal transport variability. The high degree of displacement correlation at all interrogation scales indicates that the temporal changes in shape and deformations of streamers is considerably slower than the video frame rate interval of 0.04 s, and that transport patterns can be regarded as static fields passing across the surface at this time scale. The processing methods of static background removal and the filtering of vectors using a standard deviation (noise) threshold, as developed in this study, appear to be suitable and practical for both lab and field applications. The field results further suggest that an interrogation window of 48×60 pixels^2 (scale level 8), equivalent to 108×134 mm^2 (spanwise width $\times$ streamwise length) is suitable for resolving the advection vector field of the sand transport patterns.

Future applications of the LSPIV method may require an alternative to the black cardboard screen for enhancing contrast between saltating sand and bed surface without affecting the local transport conditions. The field testing indicates a good potential for up-scaling the application to monitoring larger surface areas: the consistency in results between scale levels 8 and 10 suggests that LSPIV of transport patterns on a physical scale of ~100 mm (scale level 8 used here) can also be achieved with interrogation windows covering fewer pixels, say that of scale level 10 (24 pixels), which implies that a total surface area twice the size of the study here can be monitored with equal success. Even larger areas may be achieved with newer HD video cameras that can capture imagery at higher pixel resolutions. A key logistical challenge at these larger scales, however, may be the requirement of a fixed camera mounting platform at higher elevations while remaining stable in strong winds.

The streamer advection speeds measured at Camber Sands show a high variability across small spatial and temporal scales and generally range between 3 to 7 m s^{-1}. Because the streamers are detached from their transport surface by the cardboard screen these speeds can be interpreted as the characteristic horizontal flight velocities of the saltating grains that constitute the transport patterns. The advection speeds over the course of a 144 second period exhibit a normal distribution with a mean of 4.01 m s^{-1} and a standard deviation of 1.55 m s^{-1}, at scale level 8. The high spatio-temporal variability and the absence of any correlation between advection speeds and grain cloud densities (on both local and global scale), suggest that the small-scale dynamics and interactions of sand transport and streamer progression are not coupled to the larger-scale general wind field, but that direct turbulent eddy forcing at the streamer scale may exert an overriding control.

Acknowledgments

We are very grateful for the particularly supportive comments and constructive suggestions from two anonymous reviewers as well as the handling editor, which have significantly helped improve this manuscript.

This research was made possible by The Nuffield Foundation, through an award to AB (award NAL/01024/G). The initial version of the LSPIV algorithm was developed when AB hosted FvdB on an internship for his MSc studies at Ecole Normale Supérieure (ENS), Paris.

References

Baas, A.C.W. (2008) Challenges in aeolian geomorphology: investigating aeolian streamers. *Geomorphology*, 93, 3–16; doi: 10.1016/j.geomorph.2006.12.015.

Baas, A.C.W. (2006) Wavelet power spectra of aeolian sediment transport by boundary layer turbulence. *Geophysical Research Letters*, 33, L05403; doi:10.1029/2005GL025547.

Baas, A.C.W., and Sherman, D.J. (2005) Formation and behavior of aeolian streamers. *Journal of Geophysical Research*, 110, F03011; doi:10.1029/2004JF000270.

Baas, A.C.W. (2004) Evaluation of Saltation Flux Impact Responders (Safires) for measuring instantaneous aeolian sand transport rates. *Geomorphology*, 59, 99–118; doi:10.1016/j.geomorph.2003.09.009.

Baas, A.C.W. (2003) *Formation and Behavior of Aeolian Sand Streamers.* PhD Dissertation, Department of Geography, University of Southern California, Los Angeles, 412 p.

Bauer, B. O., J. Yi, S. L. Namikas and D. J. Sherman (1998), Event detection and conditional averaging in unsteady aeolian systems, *J. Arid Environ.*, 39, 345–375.

Bauer, BO, Walker, IJ, Baas, ACW, Jackson, DWT, McKenna-Neuman, C, Wiggs, GFS, and Hesp, PA (2013) Critical Reflections on the Coherent Flow Structures Paradigm in Aeolian Geomorphology. Chapter 8 in: Venditti, JG, Best, JL, Church, M, Hardy, RJ (eds.) *Coherent Structures in Flows at the Earth's Surface*, Wiley-Blackwell, pp.111-134.

Bauer, B. O., and R. G. D. Davidson-Arnott (2014), Aeolian particle flux profiles and transport unsteadiness. *J. Geophys. Res. Earth Surf.*, 119, 1542–1563, doi:10.1002/2014JF003128.

Bradley, A. A., A. Kruger, E. A. Meselhe, and M. V. I. Muste, (2002) Flow measurement in streams using video imagery. *Water Resour. Res.*, 38(12), 1315, doi:10.1029/2002WR001317, 2002.

Butterfield, G. R. (1998) Transitional behavior of saltation: Wind tunnel observations of unsteady winds, *J. Arid Environ.*, 39, 377– 394.

Cui, B., Komar, P.D., and Baba, J. (1983) Settling velocities of natural sand grains in air. *Journal of Sedimentary Petrology*, 53, 1205– 1211.

Davidson-Arnott, R.G.D., and Bauer, B.O. (2009) Aeolian sediment transport on a beach: Thresholds, intermittency, and high frequency variability. *Geomorphology*, 105(1-2), 117–126.

Davidson-Arnott, R., Bauer, B.O., Walker, I.J., Hesp, P.A., Ollerhead, J., and Delgado-Fernandez, I. (2009) Instantaneous and mean aeolian sediment transport rate on beaches: an intercomparison of measurements from two sensor types. *Journal of Coastal Research*, 56, 297–301.

Dong, Z., Liu, X., Wang, X., Li, F., and Zhao, A. (2004) Experimental investigation of the velocity of a sand cloud blowing over a sandy surface. *Earth Surface Processes and Landforms*, 29, 343–358.

Dong, Z., Wang, H., Zhang, X., and Ayrault, M. (2003) Height profile of particle concentration in an aeolian saltating cloud: A wind tunnel investigation by PIV MSD. *Geophysical Research Letters*, 30, 2004, 10.1029/2003GL017915.

Dong, Z., Wang, H., Liu, X., and Zhao, A. (2002) Velocity profile of a sand cloud blowing over a gravel surface. *Geomorphology*, 45 (3–4), 277–289.

Ellis, J.T., Morrison, R.F., and Priest, B.H. (2009) Detecting impacts of sand grains with a microphone system in field conditions. *Geomorphology*, 105(1-2), 87–94.

Ettema, R., Fujita, I., Muste, M., and Kruger, A. (1997) Particle-image velocimetry for whole-field measurement of ice velocities. *Cold Regions Science and Technology*, 26, 97–112.

Farrell, E.J. and Sherman, D.J. (2006) Process-scaling issues for aeolian transport modelling in field and wind tunnel experiments: Roughness length and mass flux distributions. *Journal of Coastal Research* SI 39, 384-389

Fujita, I., Muste, M., and Kruger, A. (1998) Large-scale particle image velocimetry for flow analysis in hydraulic engineering applications. *Journal of Hydraulic Research*, 36, 397–414.

Graf, W.H. (1971) *Hydraulics of Sediment Transport*. McGraw-Hill, New York.

Greeley, R., Blumberg, D.G., and Williams, S.H. (1996) Field measurements of the flux and speed of wind-blown sand. *Sedimentology*, 43, 41– 52.

Hugenholtz, C.H., Barchyn, T.E., 2011. Laboratory and field performance of a laser particle counter for measuring aeolian sand transport. *J. Geophys. Res.: Earth Surf.* 116, F01010.

Kang, L., Guo, L., Gu, Z., and Liu, D. (2008) Wind tunnel experimental investigation of sand velocity in aeolian sand transport. *Geomorphology*, 97, 438–450.

Lewis, Q. W., and B. L. Rhoads (2015), Resolving two-dimensional flow structure in rivers using large-scale particle image velocimetry: An example from a stream confluence. *Water Resour. Res.*, 51, 7977–7994, doi:10.1002/2015WR017783.

Lynch, K., Delgado-Fernandez, I., Jackson, D.W.T., Cooper, J.A.G., Baas, A.C.W., Beyers, J.H.M. (2013) Alongshore variation of aeolian sediment transport on a beach under offshore winds. *Aeolian Research* 8, 11–18.

Ma G S and Zheng X J (2011) The fluctuation property of blown sand particles and the wind-sand flow evolution studied by numerical method. *Eur. Phys. J. E* 34, 54.

Muste, M., Fujita, I., and Hauet, A. (2008) Large-scale particle image velocimetry for measurements in riverine environments. *Water Resources Research*, 44, W00D19.

Nalpanis, P., Hunt, J.C.R., and Barrett, C.F. (1993) Saltating particles over flat beds. *Journal of Fluid Mechanics*, 251, 661–685.

Namikas, S.L. (2003) Field measurement and numerical modelling of aeolian mass flux distributions on a sandy beach. *Sedimentology*, 50, 303–326.

Namikas, S.L. (2006) A conceptual model of energy partitioning in the collision of saltating grains with an unconsolidated sediment bed. *Journal of Coastal Research*, 22, 1250–1259.

Poortinga, A., Keijsers, J., Visser, S., Riksen, M., Baas, A. (2015) Temporal and spatial variability in event scale aeolian transport on Ameland, the Netherlands. *Geo Res J* 5, 23–35.

Raffel, M., Willert, C.E., and Kompenhans, J. (2001) *Particle Image Velocimetry: A Practical Guide*. Springer, Berlin, 269p.

Rasmussen, K.R., and Sørensen, M. (2008) Vertical variation of particle speed and flux density in aeolian saltation: Measurement and modelling. *Journal of Geophysical Research*, 113, F02S12, doi:10.1029/2007JF000774.

Rice, M., Willetts, B.B., and McEwan, I.K. (1996) Observation of collisions of saltating grains with a granular bed from high-speed cine-film. *Sedimentology*, 43, 21–31.

Rice, M., Willetts, B.B., and McEwan, I.K. (1995) An experimental study of multiple grain-size ejecta produced by collisions of saltating grains with a flat bed. *Sedimentology*, 42, 95–706.

Schönfeldt, H.J. (2012) High resolution sensors in space and time for determination of saltation and creep intensity. *Earth Surf. Proc. Land.* 37, 1065–1073.

Schwanghart, W (2013) Experimental (Semi-) Variogram. Mathworks File Exchange.

Sherman, D.J., and Farrell, E.J. (2008) Aerodynamic roughness lengths over movable beds: Comparison of wind tunnel and field data. *Journal of Geophysical Research*, 113, F02S08.

Sherman, D.J., Li, B., Ferrell E.J., Ellis, J.T., Cox, W.D., Maia, L.P., and Sousa, P.H.G.O. (2011) Measuring Aeolian Saltation: A Comparison of Sensors. *Journal of Coastal Research*, SI 59, 280-290

Sherman, DJ, Houser, C, Ellis, JT, Farrell, EJ, Li, B, Davidson-Arnott, RGD, Baas, ACW, and Maia, LP (2013) Characterization of aeolian streamers using time-averaged videography. *Journal of Coastal Research*, SI 65, 1331-1336

Sterk, G., A. F. G. Jacobs and J. H. van Boxel (1998), The effect of turbulent flow structures on saltation sand transport in the atmospheric boundary layer, *Earth Surf. Process. Landf.*, 23, 877–887.

Sutarto, T.E. (2015) Application of large scale particle image velocimetry (LSPIV) to identify flow pattern in a channel. *Procedia Engineering* 125, 213–219.

Udo, K. (2009) Field measurement of seasonal wind-blown sand flux using high-frequency sampling instrumentation. *Journal of Coastal Research*, 56, 148–152.

Walker, I.J., Hesp, P.A., Davidson-Arnott, R.G.D., Bauer, B.O., Namikas, S.L., and Ollerhead, J. (2009) Responses of three-dimensional flow to variations in the angle of incident wind and profile form of dunes: Greenwich Dunes, Prince Edward Island, Canada. *Geomorphology*, 105(1-2), 127–138.

Wang, D., Wang, Y., Yang, B., and Zhang, W. (2008) Statistical analysis of sand grain/bed collision process recorded by high-speed digital camera. *Sedimentology*, 55, 461–470.

Westerweel, J. (1997) Fundamentals of digital particle image velocimetry. *Measurement Science and Technology*, 8, 1379–1392.

White, B.R., and Schulz, J.C. (1977) Magnus effect on saltation. *Journal of Fluid Mechanics*, 81, 497–512.

Wiggs, G.F.S. & Weaver, C.M. (2012) Turbulent flow structures and aeolian sediment transport over a barchan sand dune. *Geophys. Res. Lett.*, 39, L05404, doi:10.1029/. 2012GL050847.

Yang, P., Dong, Z., Qian, G., Luo, W., and Wang, H. (2007) Height profile of the mean velocity of an aeolian saltating cloud: Wind tunnel measurements by Particle Image Velocimetry. *Geomorphology*, 89, 320–334.

Zhang, W., Wang, Y., and Lee, S-J. (2007) Two-phase measurements of wind and saltating sand in an atmospheric boundary layer. *Geomorphology*, 88, 109–119.

Figure Captions

Figure 1: Conceptualization of the LSPIV algorithm applied to a frame-pair showing advection of a streamer (dark shape) moving toward the upper-left. *S* is source interrogation window at location (*x*, *y*) on first frame, which is matched to potential destination windows on the second frame (two examples shown, *D* and *D*□) within a defined searching area (indicated). The match between *S* and *D* yields an optimum correlation, the match between *S* and *D*□ a very low correlation. Another example of an optimum match is shown between *s* and *d*.

Figure 2: Laboratory testing of the LSPIV method on vertical grain fall in front of a black background screen: (a) two upper-left images showing the consecutive RGB frames from the video sequence, (b) two lower-left images displaying the corresponding sand signal extracted from the static background, (c) right-hand two images showing the PIV displacement vectors overlain over the first frame, for scale level 6 (c1, top) and level 9 (c2, bottom); vector lengths are scaled by 0.5 for clarity; axes in m. [colour version online]

Figure 3: Histogram distributions of the cross-correlation coefficients for filtered displacement vectors, from all 100 frame-pairs in the laboratory video sequence, for each scale level. Each histogram is annotated with distribution statistics in the top-left corner.

Figure 4: Histogram distributions of the vertical downward velocities (m s^{-1}) measured in the laboratory video sequence, from all 100 frame-pairs, at each scale level. Each histogram is annotated with distribution statistics in the top-left corner.

Figure 5: Weighted means (symbols) and standard deviations (surrounding error bars) of the vertical downward velocity analysed for top-half and bottom-half of the laboratory video imagery separately, for each interrogation scale.

Figure 6: Field deployment of the LSPIV method on the back beach at Camber Sands, UK, 20 May 2006: (a) aeolian sand streamers moving toward the observer, (b) the experimental set-up with the video camera suspended from a metal frame viewing downward onto a black cardboard surface aligned with the transport direction. [colour version online]

Figure 7: Field application of the LSPIV method on aeolian streamers: (a) top-left showing the two consecutive RGB frames from the video sequence, (b) top-right displaying the sand signal extracted from these frames; signal intensity scale shown in colourbar on the right, (c) bottom-left showing the PIV displacement vectors overlain over the first frame, for scale level 4 (upper pane) and level 8 (lower pane); vector lengths are scaled by 0.7 for clarity; axes in m; a sample of the interrogation window is shown in black outline, (d) bottom-right indicating the correlation coefficients for the displacement vectors in coloured blocks centred at each vector source point; colourbar legend on the right [colour version online]

Figure 8: Histogram distributions of the cross-correlation coefficients for filtered displacement vectors from all 3600 frame-pairs in the field video sequence, for each scale level. Each histogram is annotated with distribution statistics in the top-left corner.

Figure 9: Histogram distributions of the scalar advection speeds (m s^{-1}) measured in the field, from all 3600 frame-pairs, at each scale level. Each histogram is annotated with distribution statistics in the top-left corner.

Figure 10: Time-series of mean scalar advection speed (m s^{-1}) for the entire 144 s (3600 frames) footage sequence, resolved at scale level 5. Gaps in the time-series indicate periods where no velocities were measurable.

Figure 11: Two selected shorter periods of the 144 s footage sequence, resolved at scale level 8: (a) 28 s period early on in the sequence, (b) 12 s period at the end of the sequence. Graphs show time-series of weighted means (symbols and bold line) and standard deviations (lighter coloured error-bars) of scalar advection speeds (m s^{-1}), on the upper-left axis, advection direction (compass degrees) relative to *x*-direction of frame, on the right-side axis, and the number of qualifying vectors available per frame (lower solid line), on the lower-left axis. [colour version online]

Figure 12: Scatter plot of the advection speeds of individual vectors versus the mean sand signal (pixel values) in their associated interrogation windows (averaged between source and destination window), at scale level 8, for the 28 s shown in Figure 11a. The point cloud shown here is a 10% sample of the full population of individual vector measurements, noted as N in the top-right corner. Grey-scale intensities indicate the correlation coefficient associated with the vector measurement (darker = higher *r*).

Figure 13: Scatter plot of the mean advection speed at scale level 8 per individual frame versus the image-wide mean sand signal present, for the period shown in Figure 11a.

Figure 14: Spatial coherence of the sand transport patterns: 2D variograms for (a) a 5-second sequence (37-42 seconds) in the period of Figure 11a, and (b) for a 2-second sequence (133-135 s) in the period of Figure 11b; spatial variance colourbar scale on the right, (c) 1D variograms extracted from Figure 14b showing spatial variance as a function of spanwise (in blue) and streamwise (in red) separation distance.

Figure 15: Spatio-temporal collage of 51 frames of extracted sand signal, covering 2 seconds (38-40s) near the start of the period shown in Figure 11a. Top-left is the first frame of the sequence and subsequent frames are overlapped using the scale level 1 (whole-frame) displacement vectors in reverse direction. Axes scaling has been converted to spatial distance in metres.

Supporting Material

Video_1_Lab_footage.mpg: Laboratory testing: the original 4-second filmed RGB footage of vertical grain fall patterns.

Video_2_Lab_level6.mp4: Laboratory testing: video sequence of the (filtered) displacement vectors drawn over the extracted sand signal at interrogation scale 6. Vector lengths are scaled by 0.7 to reduce visual overlap, and video is slowed down to 10 frames per second (from original 25 fps).

Video_3_Lab_level9.mp4: Laboratory testing: video sequence of the (filtered) displacement vectors drawn over the extracted sand signal at interrogation scale 9. Vector lengths are scaled by 0.7 to reduce visual overlap, and video is slowed down to 10 frames per second (from original 25 fps).

Video_4_Field_footage.mpg: Field experiment: a 12-second sequence of the filmed RGB footage of streamers and sand transport patterns moving over the black cardboard surface. This 12-second sequence corresponds to the period shown in Figure 11b.

Video_5_Field_level4.mp4: Field experiment: video sequence of the (filtered) displacement vectors drawn over the extracted sand signal at interrogation scale 4, for the 12-second sequence shown in Video_4. Vector lengths are scaled by 0.7 to reduce visual overlap, and video is slowed down to 10 frames per second (from original 25 fps).

Video_6_Field_level8.mp4: Field experiment: video sequence of the (filtered) displacement vectors drawn over the extracted sand signal at interrogation scale 8, for the 12-second sequence shown in Video_4. Vector lengths are scaled by 0.7 to reduce visual overlap, and video is slowed down to 10 frames per second (from original 25 fps).

Tables

Table 1: The LSPIV search algorithm parameters at each interrogation scale level, as developed in this study. See accompanying text for details.

scale level	interrogation window (pixels)		# vector locations		search radius (pixels)			first-pass step-size (pixels)
	height	width	per axis	total	in *y*	in *x*	window	
1	576	720	1	1	145	180	291×361	5
2	384	480	2	4	90	115	181×231	5
3	288	360	4	16	56	72	113×145	4
4	192	240	7	49	36	44	73×89	4
5	144	180	10	100	21	27	43×55	3
6	96	120	16	256	15	18	31×37	3
7	72	90	22	484	10	10	21×21	2
8	48	60	34	1156	10	10	22×21	2
9	36	45	46	2116	10	10	23×21	2
10	24	30	70	4900	10	10	24×21	2

Table 2: Comparing the LSPIV measured downward velocities of falling sand in the lab testing with theoretical fall velocities predicted by adjusted B.B.O. equation.

theoretical fall velocity (m s^{-1})		LSPIV measured downward velocity (m s^{-1})		difference (% of theoretical)
centre of frame	4.55	weighted mean whole frame, scale 5 and up	4.6	1.1%
centre of **top-half** of frame	4.48	weighted mean **top-half** of frame, scale 8 and up	4.54	1.3%
centre of **bottom-half** of frame	4.62	weighted mean **bottom-half** of frame, scale 8 and up	4.68	1.3%

Table 3: Statistics from the LSPIV measurement data for laboratory test and field deployment.

Laboratory test								
		cross-correlation coefficient, *r*				**downward velocity (m s^{-1})**		
scale level		median	mean	st.dev.		weighted mean	weighted st.dev.	CoV
1		0.88	0.90	0.04		4.75	0.38	0.08
2		0.87	0.88	0.05		4.76	0.51	0.11
3		0.87	0.87	0.07		4.67	0.75	0.16

4		0.85	0.83	0.09		4.67	0.84	0.18
5		0.83	0.81	0.10		4.63	0.86	0.19
6		0.79	0.76	0.13		4.60	0.90	0.20
7		0.75	0.72	0.15		4.60	0.86	0.19
8		0.68	0.65	0.18		4.62	0.85	0.18
9		0.61	0.60	0.18		4.61	0.86	0.19
10		0.54	0.55	0.18		4.60	0.84	0.18
Field deployment								
		cross-correlation coefficient, *r*				**advection speed (m s^{-1})**		
scale level		median	mean	st.dev.		weighted mean	weighted st.dev.	CoV
1		0.82	0.82	0.05		4.37	1.15	0.26
2		0.83	0.82	0.05		4.40	1.33	0.30
3		0.84	0.83	0.06		4.27	1.48	0.35
4		0.84	0.83	0.07		4.23	1.66	0.39
5		0.84	0.83	0.08		4.17	1.72	0.41
6		0.84	0.82	0.09		4.12	1.69	0.41
7		0.83	0.81	0.10		4.07	1.59	0.39
8		0.81	0.79	0.12		4.01	1.55	0.39
9		0.80	0.78	0.12		4.00	1.55	0.39
10		0.79	0.76	0.13		3.99	1.54	0.39

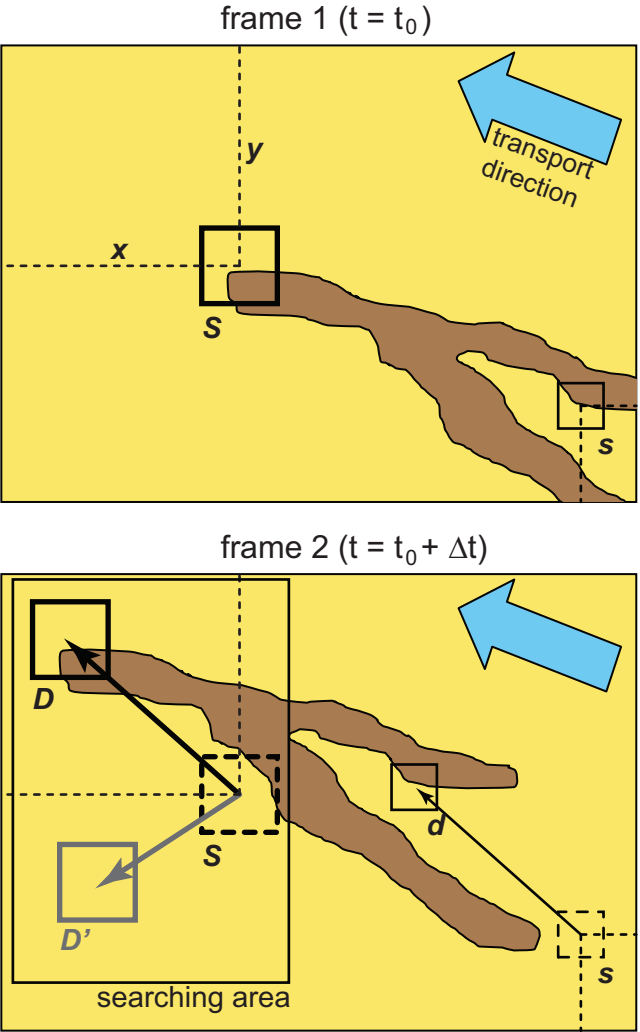
frame 1 (t = t0)
y
x
S
transport direction
s
frame 2 (t = t0 + Δt)
D
S
D'
d
s
searching area

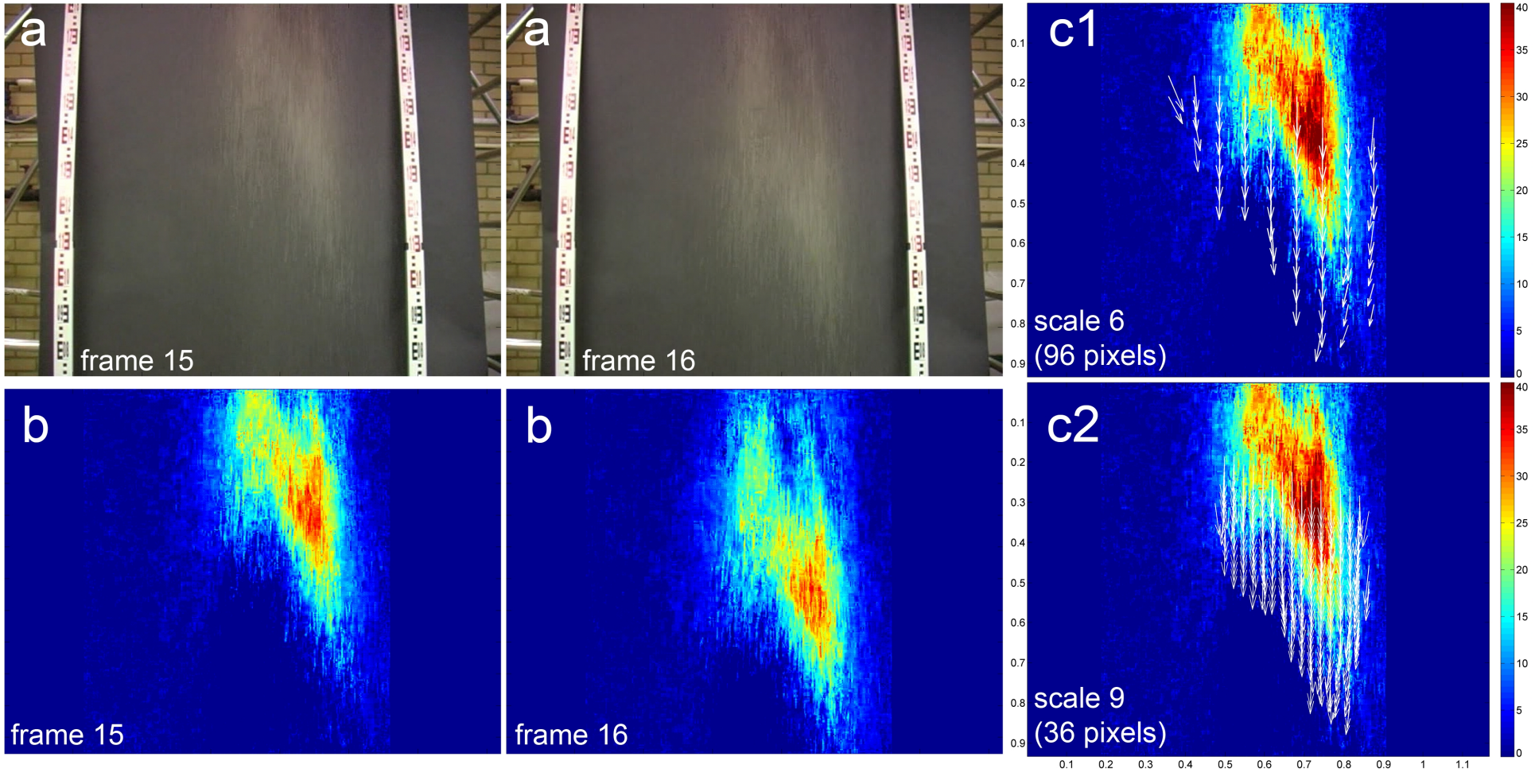
a
frame 15
a
frame 16
c1
scale 6
(96 pixels)
b
frame 15
b
frame 16
c2
scale 9
(36 pixels)
0.1
0.2
0.3
0.4
0.5
0.6
0.7
0.8
0.9
1
1.1
0
5
10
15
20
25
30
35
40

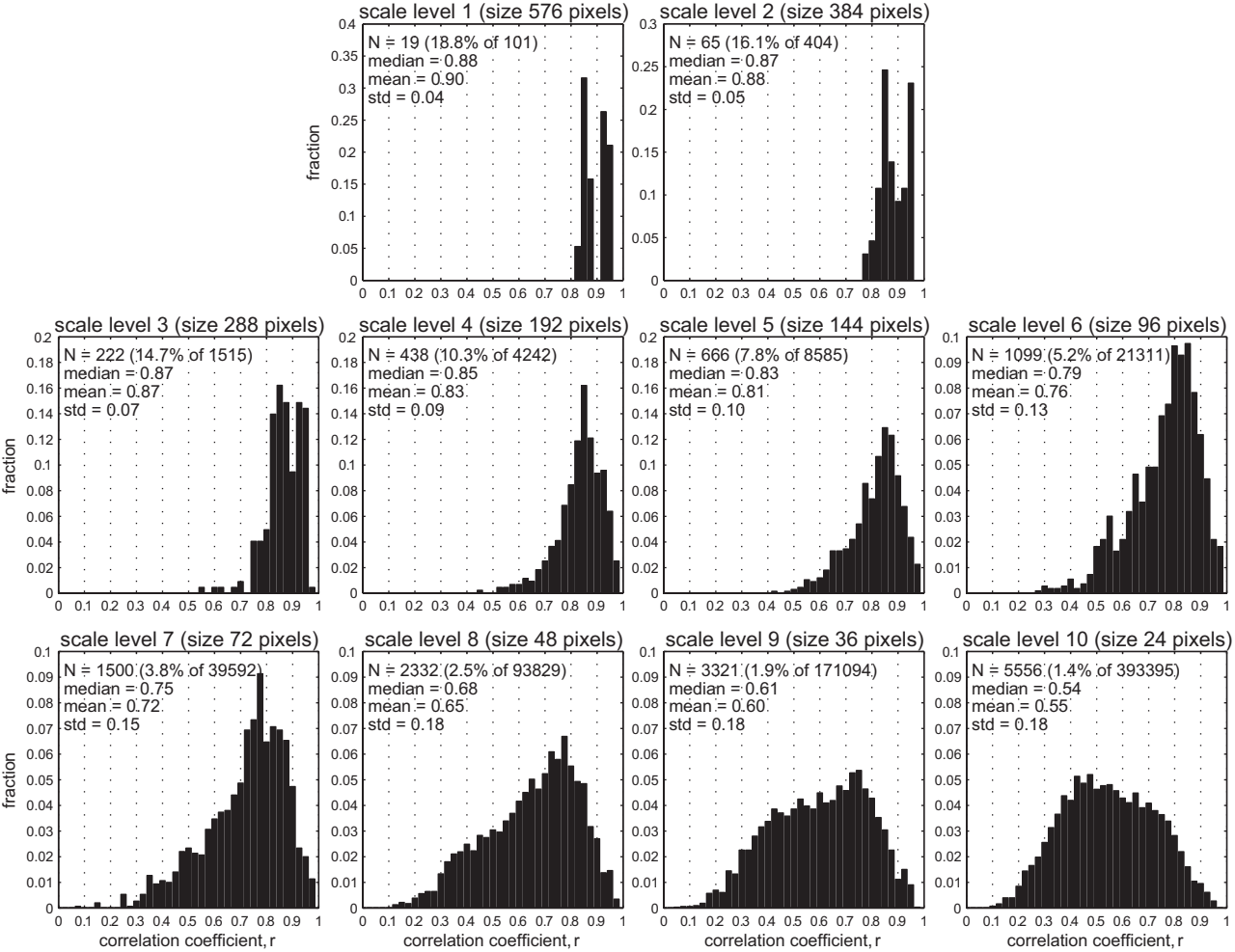
scale level 1 (size 576 pixels)
N = 19 (18.8% of 101)
median = 0.88
mean = 0.90
std = 0.04
scale level 2 (size 384 pixels)
N = 65 (16.1% of 404)
median = 0.87
mean = 0.88
std = 0.05
scale level 3 (size 288 pixels)
N = 222 (14.7% of 1515)
median = 0.87
mean = 0.87
std = 0.07
scale level 4 (size 192 pixels)
N = 438 (10.3% of 4242)
median = 0.85
mean = 0.83
std = 0.09
scale level 5 (size 144 pixels)
N = 666 (7.8% of 8585)
median = 0.83
mean = 0.81
std = 0.10
scale level 6 (size 96 pixels)
N = 1099 (5.2% of 21311)
median = 0.79
mean = 0.76
std = 0.13
scale level 7 (size 72 pixels)
N = 1500 (3.8% of 39592)
median = 0.75
mean = 0.72
std = 0.15
scale level 8 (size 48 pixels)
N = 2332 (2.5% of 93829)
median = 0.68
mean = 0.65
std = 0.18
scale level 9 (size 36 pixels)
N = 3321 (1.9% of 171094)
median = 0.61
mean = 0.60
std = 0.18
scale level 10 (size 24 pixels)
N = 5556 (1.4% of 393395)
median = 0.54
mean = 0.55
std = 0.18
fraction
correlation coefficient, r

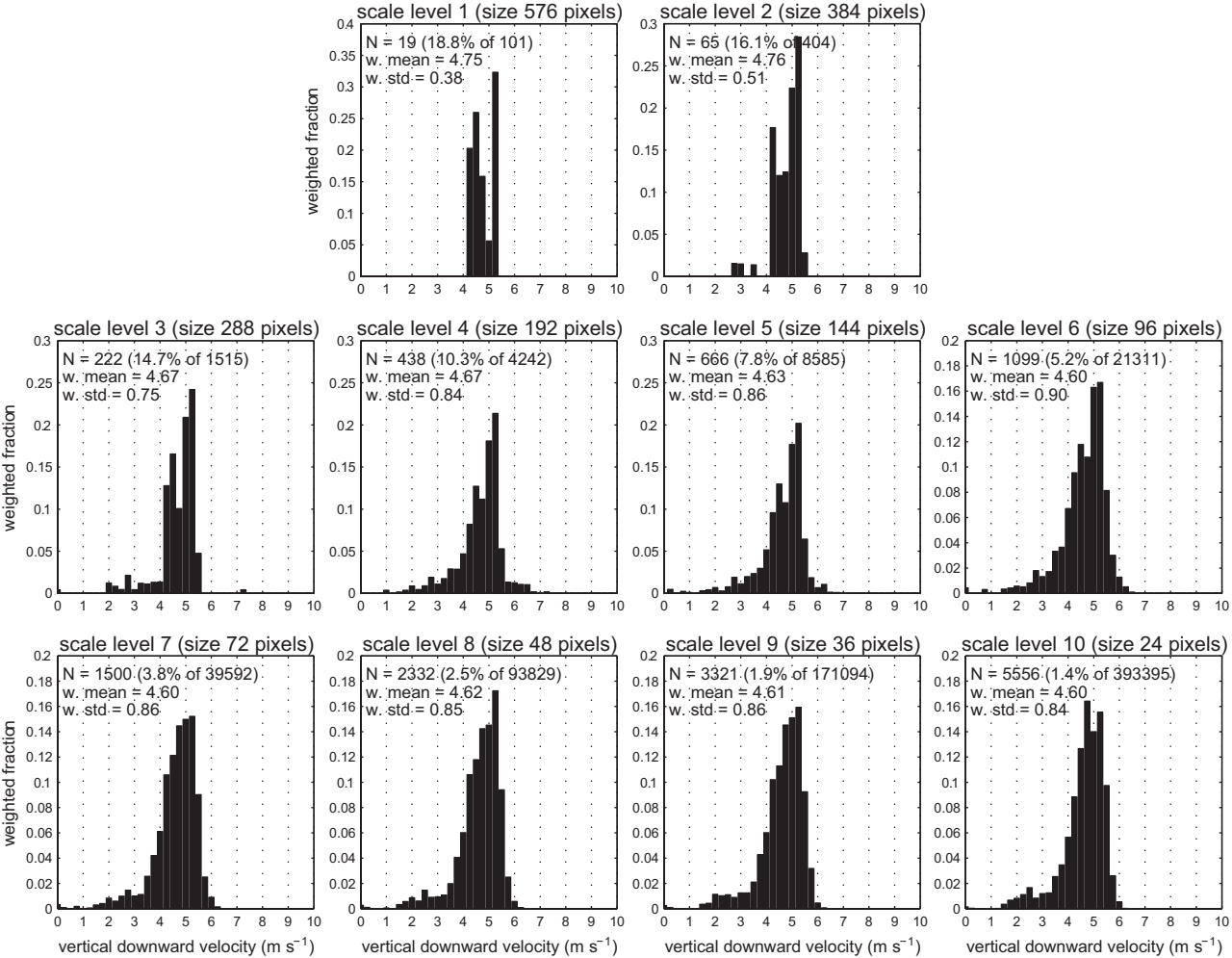
scale level 1 (size 576 pixels)
N = 19 (18.8% of 101)
w. mean = 4.75
w. std = 0.38
scale level 2 (size 384 pixels)
N = 65 (16.1% of 404)
w. mean = 4.76
w. std = 0.51
scale level 3 (size 288 pixels)
N = 222 (14.7% of 1515)
w. mean = 4.67
w. std = 0.75
scale level 4 (size 192 pixels)
N = 438 (10.3% of 4242)
w. mean = 4.67
w. std = 0.84
scale level 5 (size 144 pixels)
N = 666 (7.8% of 8585)
w. mean = 4.63
w. std = 0.86
scale level 6 (size 96 pixels)
N = 1099 (5.2% of 21311)
w. mean = 4.60
w. std = 0.90
scale level 7 (size 72 pixels)
N = 1500 (3.8% of 39592)
w. mean = 4.60
w. std = 0.86
scale level 8 (size 48 pixels)
N = 2332 (2.5% of 93829)
w. mean = 4.62
w. std = 0.85
scale level 9 (size 36 pixels)
N = 3321 (1.9% of 171094)
w. mean = 4.61
w. std = 0.86
scale level 10 (size 24 pixels)
N = 5556 (1.4% of 393395)
w. mean = 4.60
w. std = 0.84
weighted fraction
vertical downward velocity (m s^{-1})

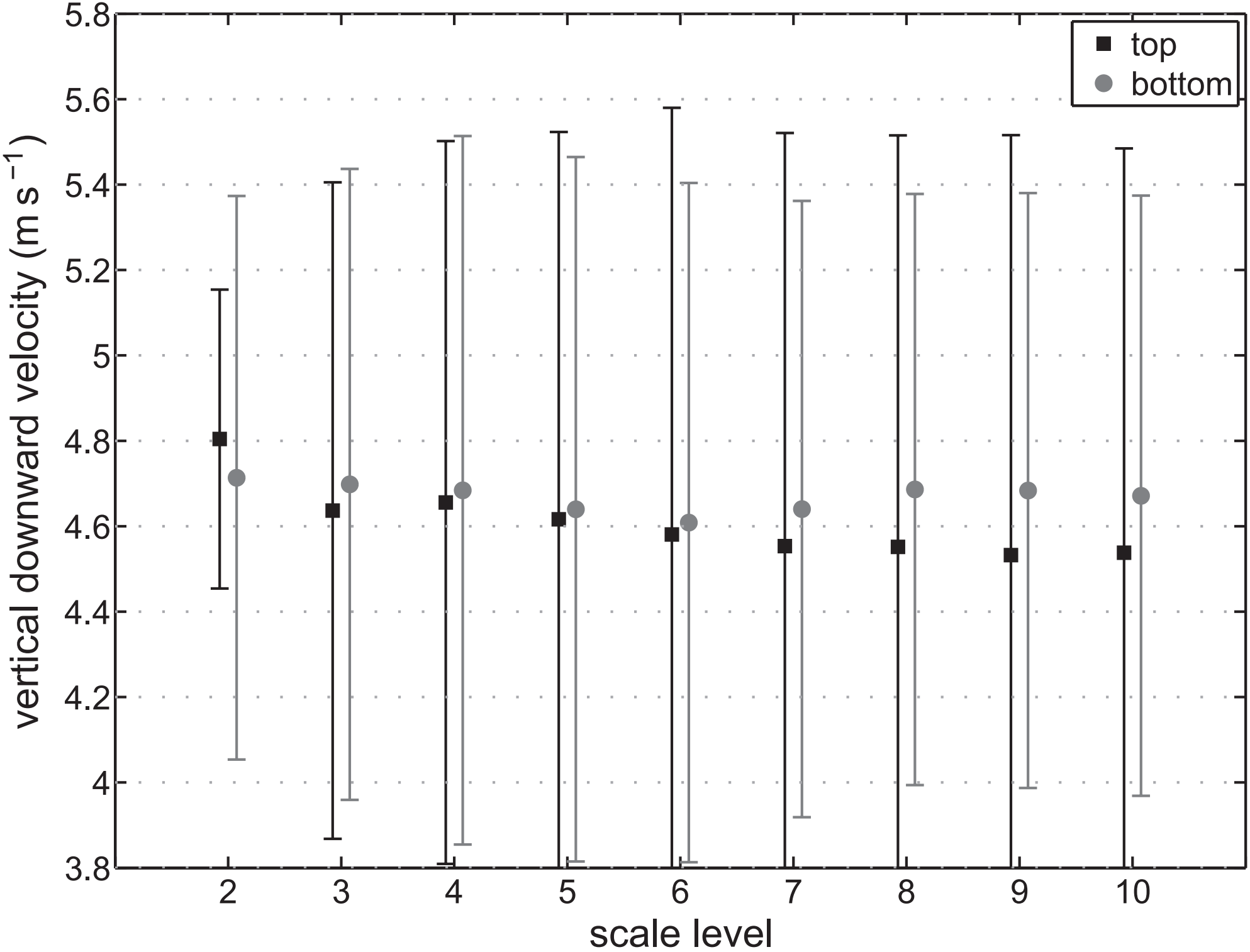
top
bottom
vertical downward velocity (m s^{-1})
scale level
5.8
5.6
5.4
5.2
5
4.8
4.6
4.4
4.2
4
3.8
2
3
4
5
6
7
8
9
10

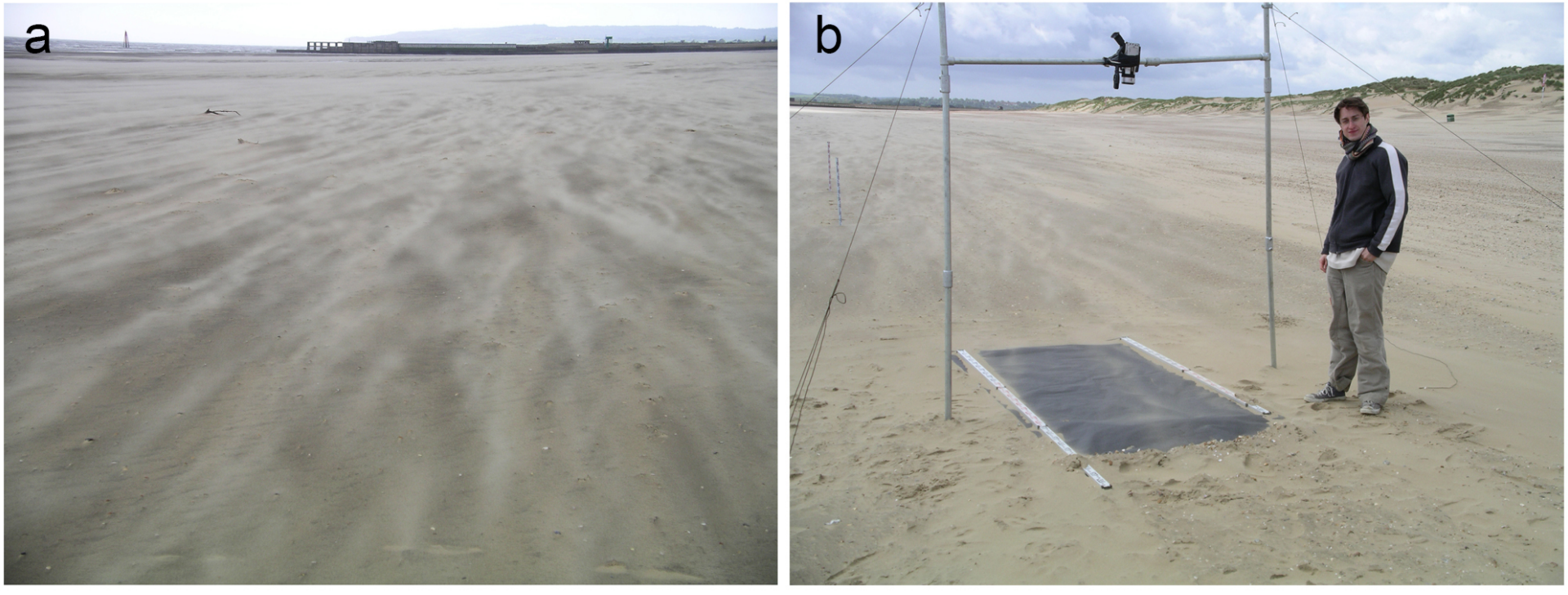
a
b

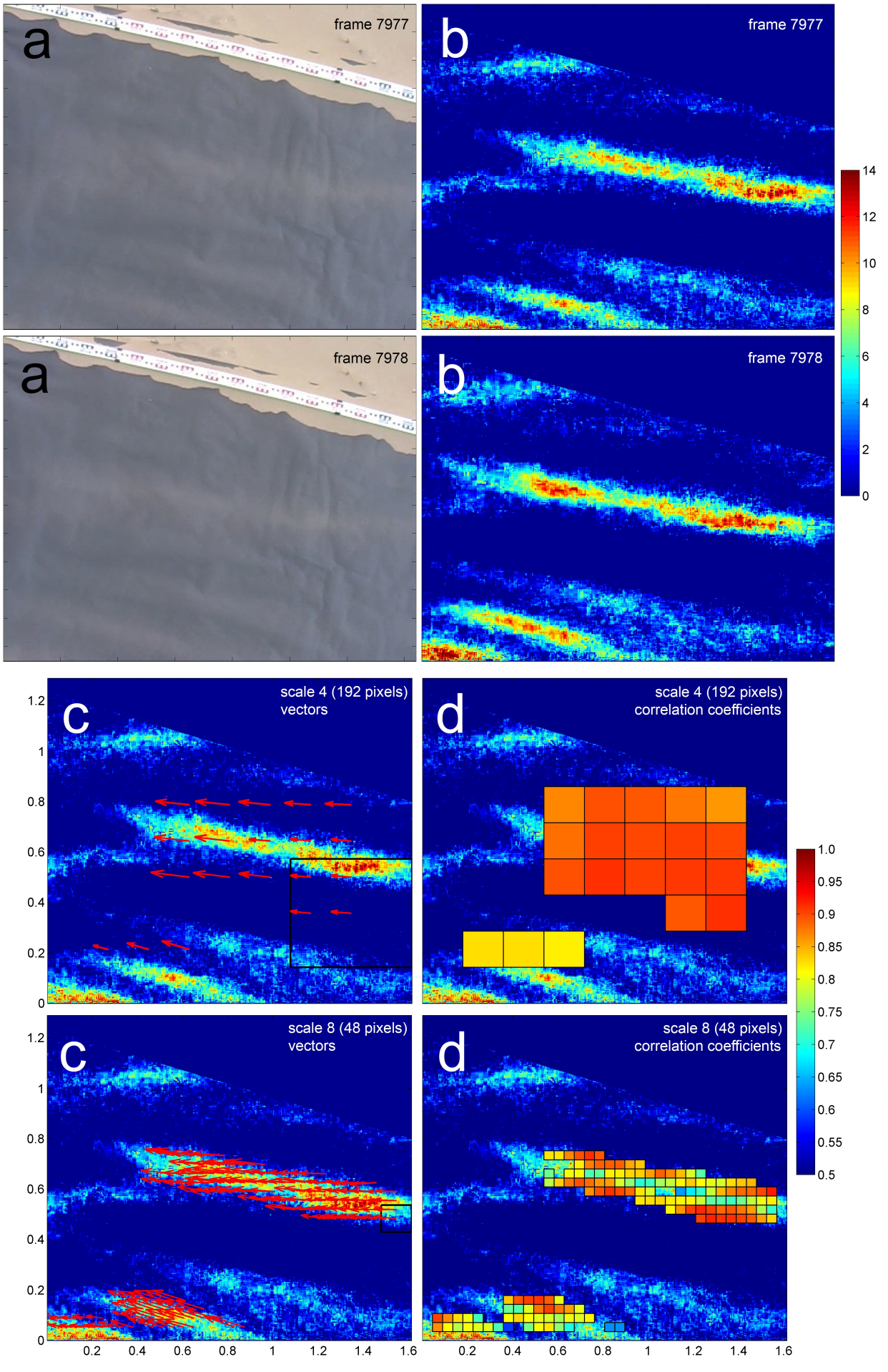
a
frame 7977
b
frame 7977
14
12
10
8
6
4
2
0
a
frame 7978
b
frame 7978
c
scale 4 (192 pixels)
vectors
d
scale 4 (192 pixels)
correlation coefficients
1.2
1
0.8
0.6
0.4
0.2
0
1.0
0.95
0.9
0.85
0.8
0.75
0.7
0.65
0.6
0.55
0.5
c
scale 8 (48 pixels)
vectors
d
scale 8 (48 pixels)
correlation coefficients
0.2
0.4
0.6
0.8
1
1.2
1.4
1.6

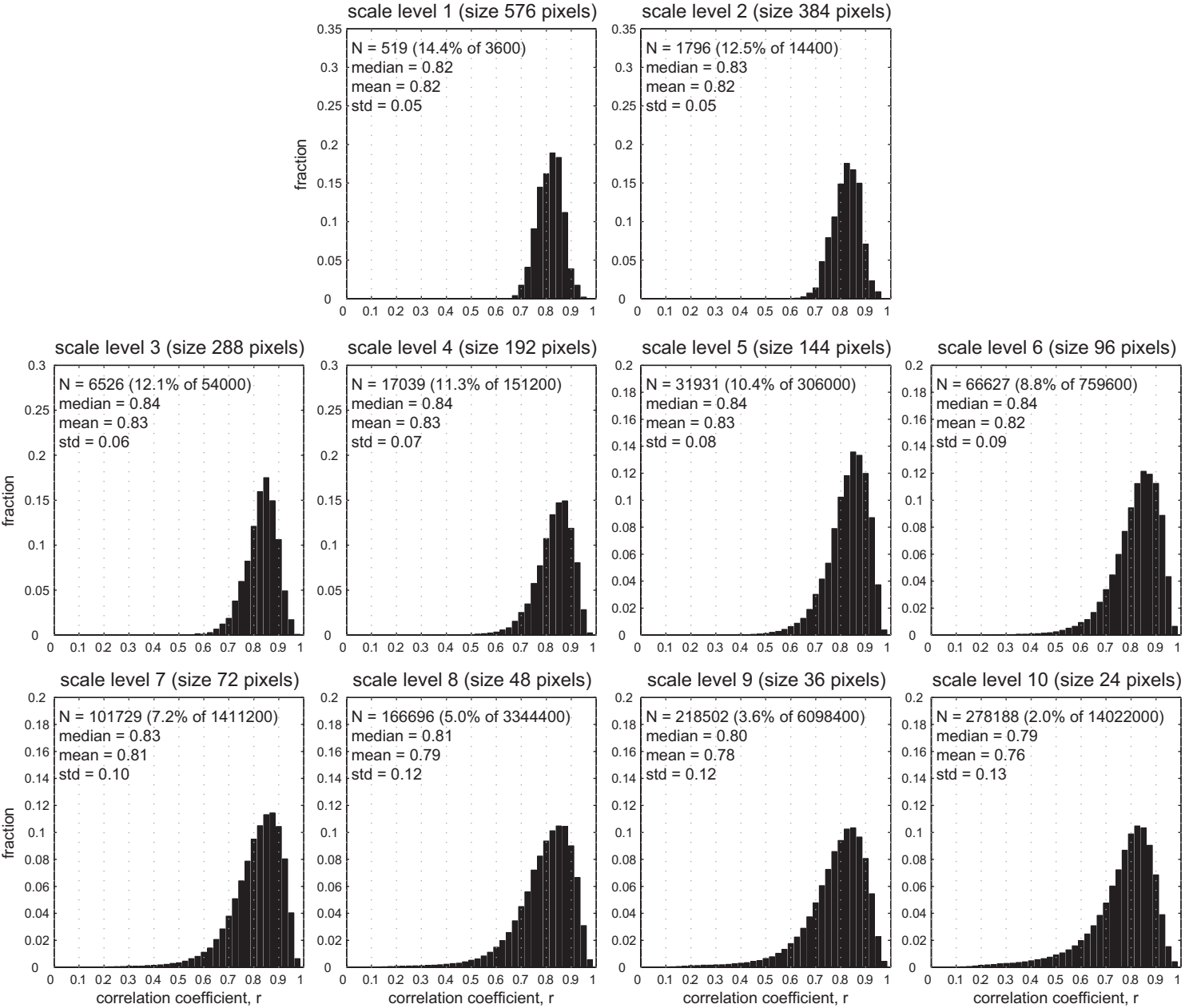
scale level 1 (size 576 pixels)
N = 519 (14.4% of 3600)
median = 0.82
mean = 0.82
std = 0.05
scale level 2 (size 384 pixels)
N = 1796 (12.5% of 14400)
median = 0.83
mean = 0.82
std = 0.05
scale level 3 (size 288 pixels)
N = 6526 (12.1% of 54000)
median = 0.84
mean = 0.83
std = 0.06
scale level 4 (size 192 pixels)
N = 17039 (11.3% of 151200)
median = 0.84
mean = 0.83
std = 0.07
scale level 5 (size 144 pixels)
N = 31931 (10.4% of 306000)
median = 0.84
mean = 0.83
std = 0.08
scale level 6 (size 96 pixels)
N = 66627 (8.8% of 759600)
median = 0.84
mean = 0.82
std = 0.09
scale level 7 (size 72 pixels)
N = 101729 (7.2% of 1411200)
median = 0.83
mean = 0.81
std = 0.10
scale level 8 (size 48 pixels)
N = 166696 (5.0% of 3344400)
median = 0.81
mean = 0.79
std = 0.12
scale level 9 (size 36 pixels)
N = 218502 (3.6% of 6098400)
median = 0.80
mean = 0.78
std = 0.12
scale level 10 (size 24 pixels)
N = 278188 (2.0% of 14022000)
median = 0.79
mean = 0.76
std = 0.13
fraction
correlation coefficient, r

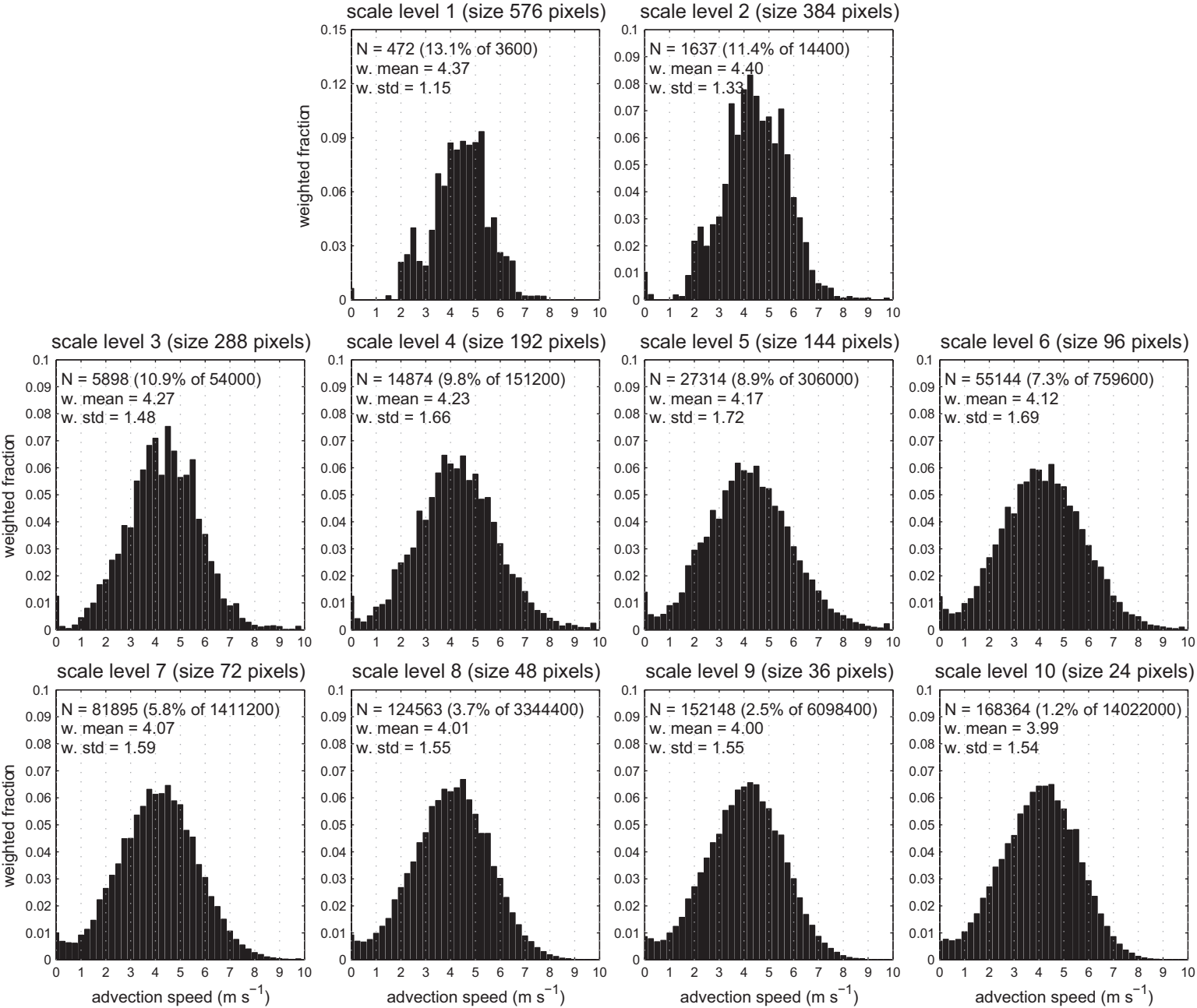
scale level 1 (size 576 pixels)
N = 472 (13.1% of 3600)
w. mean = 4.37
w. std = 1.15
scale level 2 (size 384 pixels)
N = 1637 (11.4% of 14400)
w. mean = 4.40
w. std = 1.33
scale level 3 (size 288 pixels)
N = 5898 (10.9% of 54000)
w. mean = 4.27
w. std = 1.48
scale level 4 (size 192 pixels)
N = 14874 (9.8% of 151200)
w. mean = 4.23
w. std = 1.66
scale level 5 (size 144 pixels)
N = 27314 (8.9% of 306000)
w. mean = 4.17
w. std = 1.72
scale level 6 (size 96 pixels)
N = 55144 (7.3% of 759600)
w. mean = 4.12
w. std = 1.69
scale level 7 (size 72 pixels)
N = 81895 (5.8% of 1411200)
w. mean = 4.07
w. std = 1.59
scale level 8 (size 48 pixels)
N = 124563 (3.7% of 3344400)
w. mean = 4.01
w. std = 1.55
scale level 9 (size 36 pixels)
N = 152148 (2.5% of 6098400)
w. mean = 4.00
w. std = 1.55
scale level 10 (size 24 pixels)
N = 168364 (1.2% of 14022000)
w. mean = 3.99
w. std = 1.54
weighted fraction
advection speed (m s^{-1})

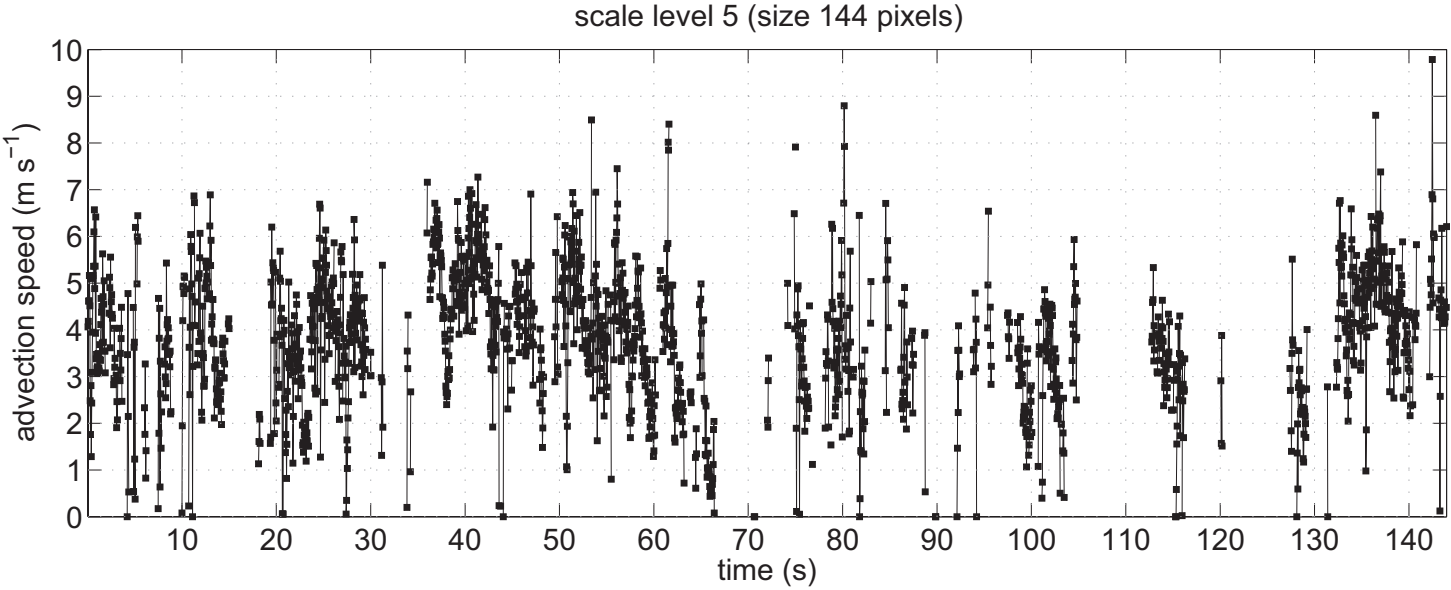
scale level 5 (size 144 pixels)
advection speed (m s^{-1})
time (s)
0
1
2
3
4
5
6
7
8
9
10
10
20
30
40
50
60
70
80
90
100
110
120
130
140

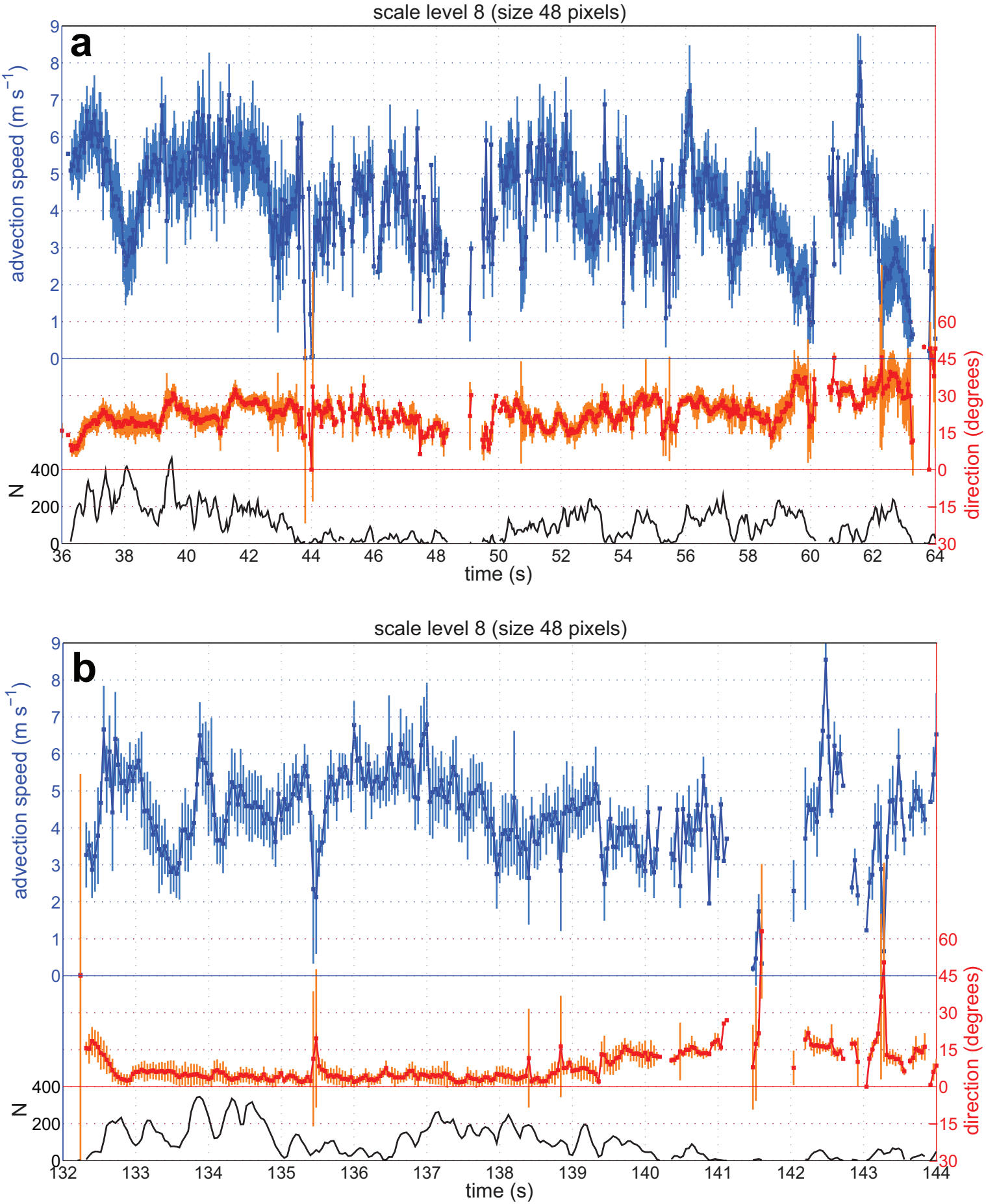
scale level 8 (size 48 pixels)
a
advection speed (m s^{-1})
direction (degrees)
N
time (s)
scale level 8 (size 48 pixels)
b
advection speed (m s^{-1})
direction (degrees)
N
time (s)

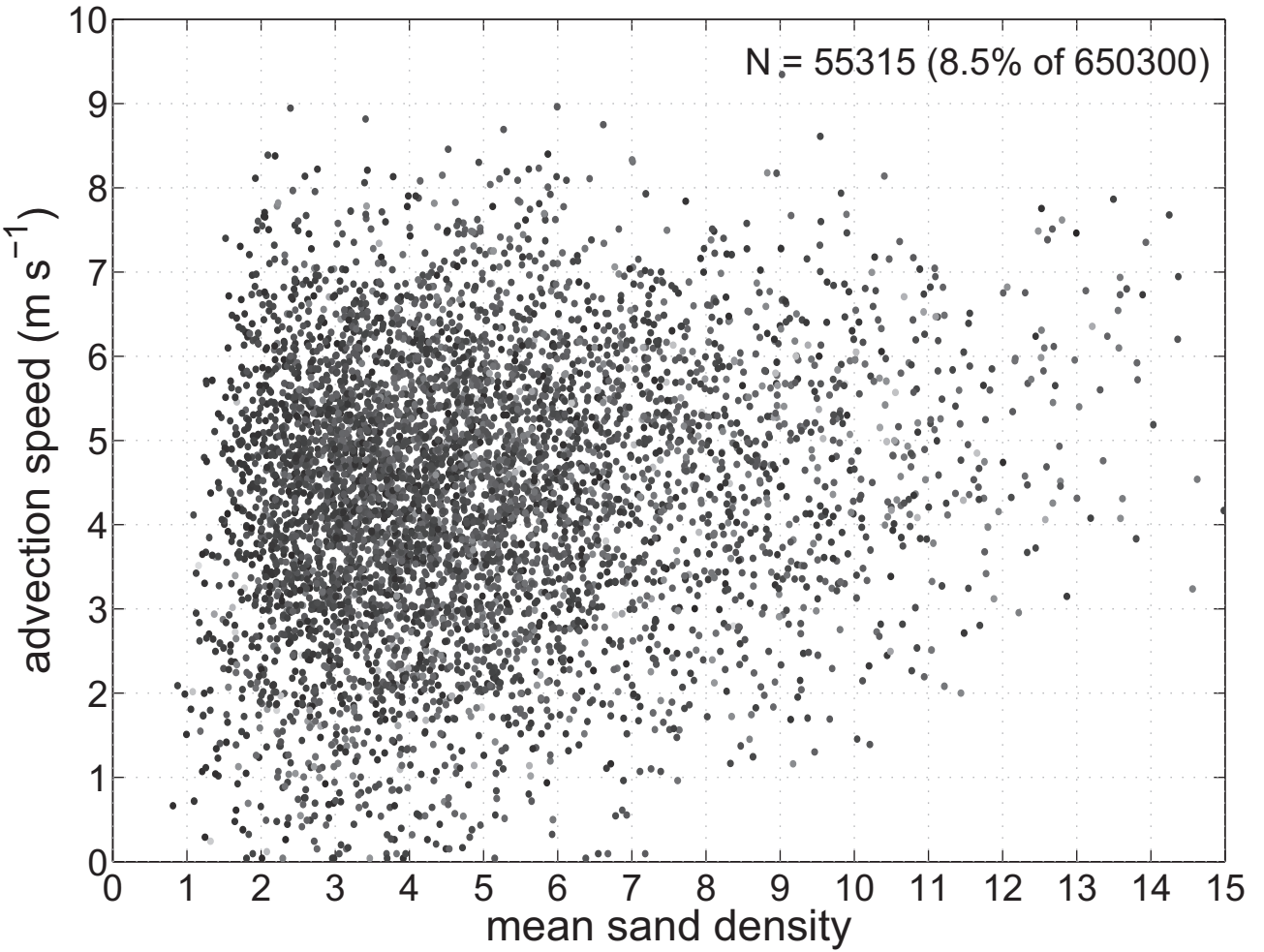
scale level 8 (size 48 pixels)
N = 55315 (8.5% of 650300)
advection speed (m s^{-1})
mean sand density
0
1
2
3
4
5
6
7
8
9
10
11
12
13
14
15

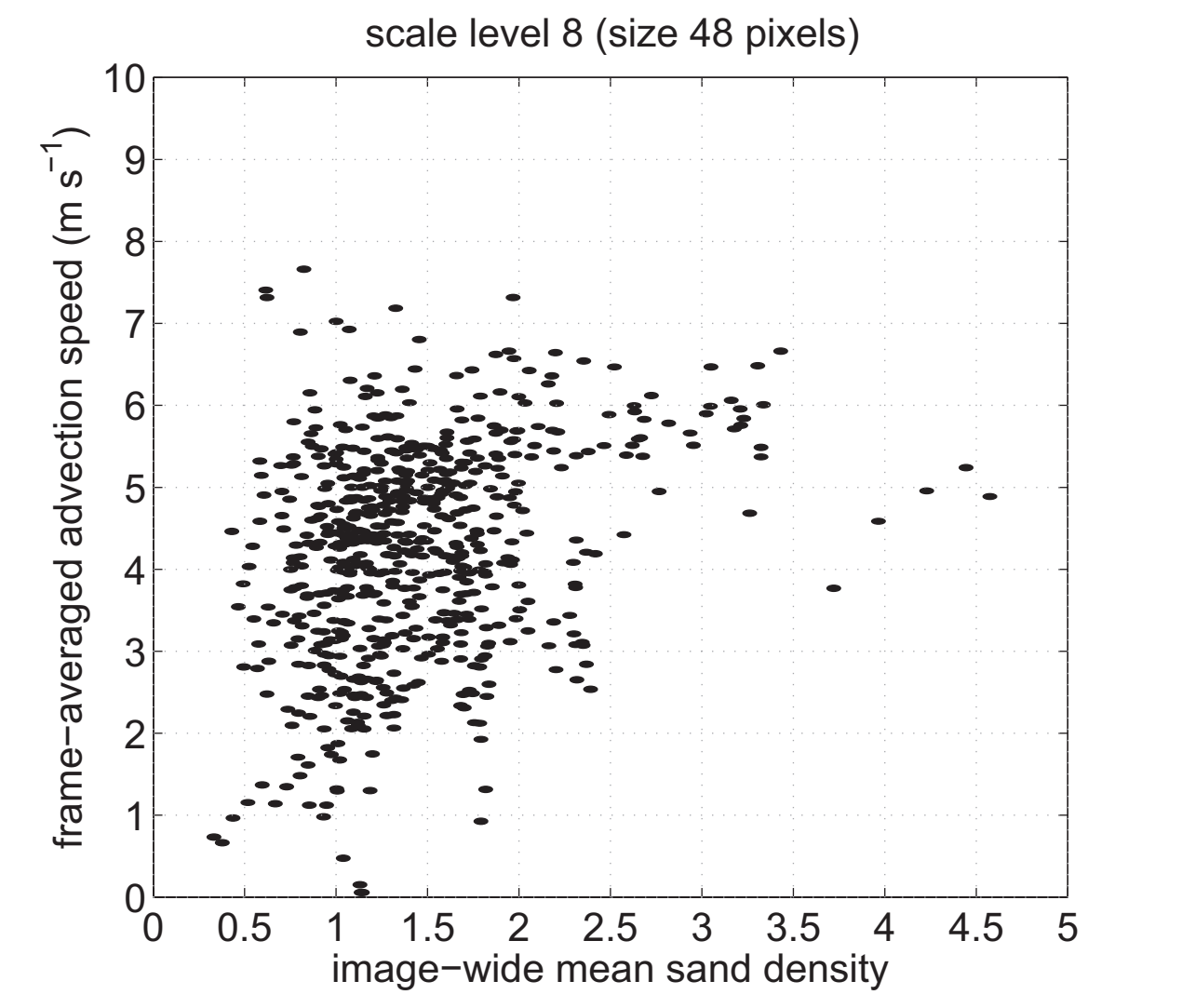
scale level 8 (size 48 pixels)
frame−averaged advection speed (m s^{-1})
image−wide mean sand density
0
1
2
3
4
5
6
7
8
9
10
0
0.5
1
1.5
2
2.5
3
3.5
4
4.5
5

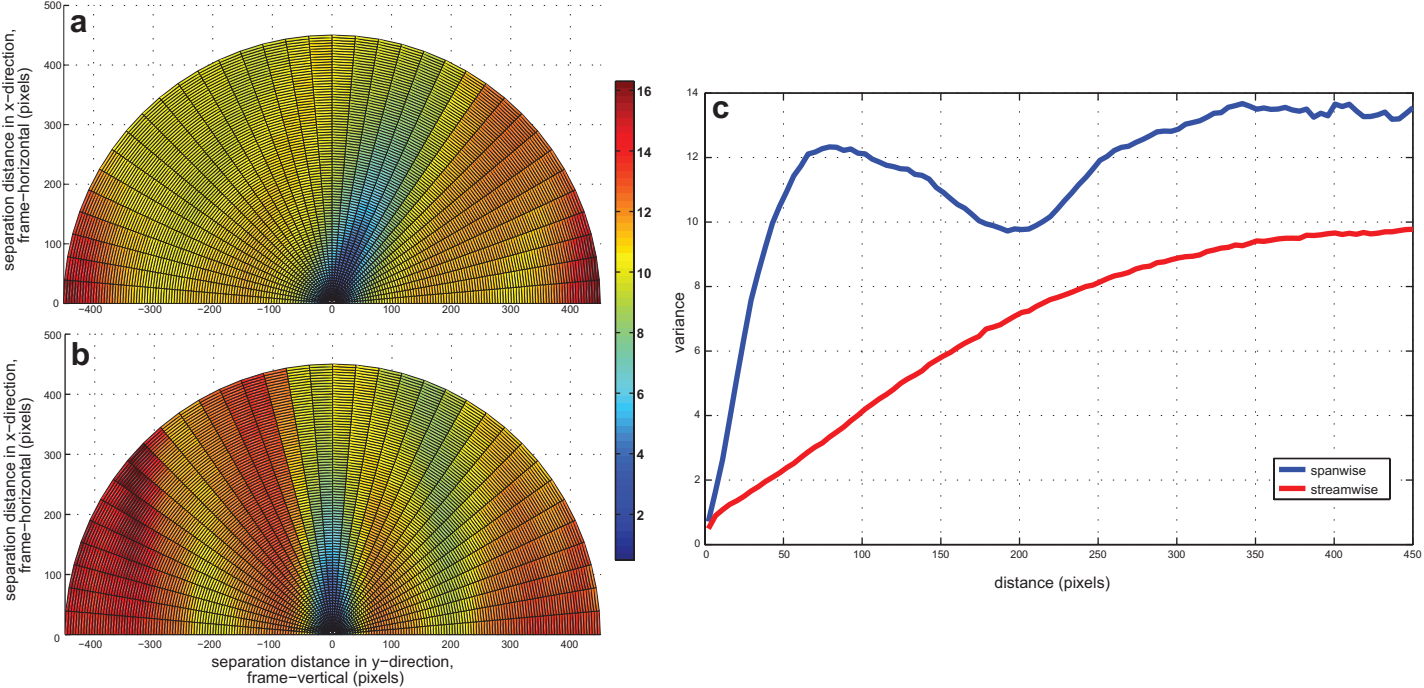
a
b
c
separation distance in x−direction, frame−horizontal (pixels)
separation distance in y−direction, frame−vertical (pixels)
variance
distance (pixels)
spanwise
streamwise

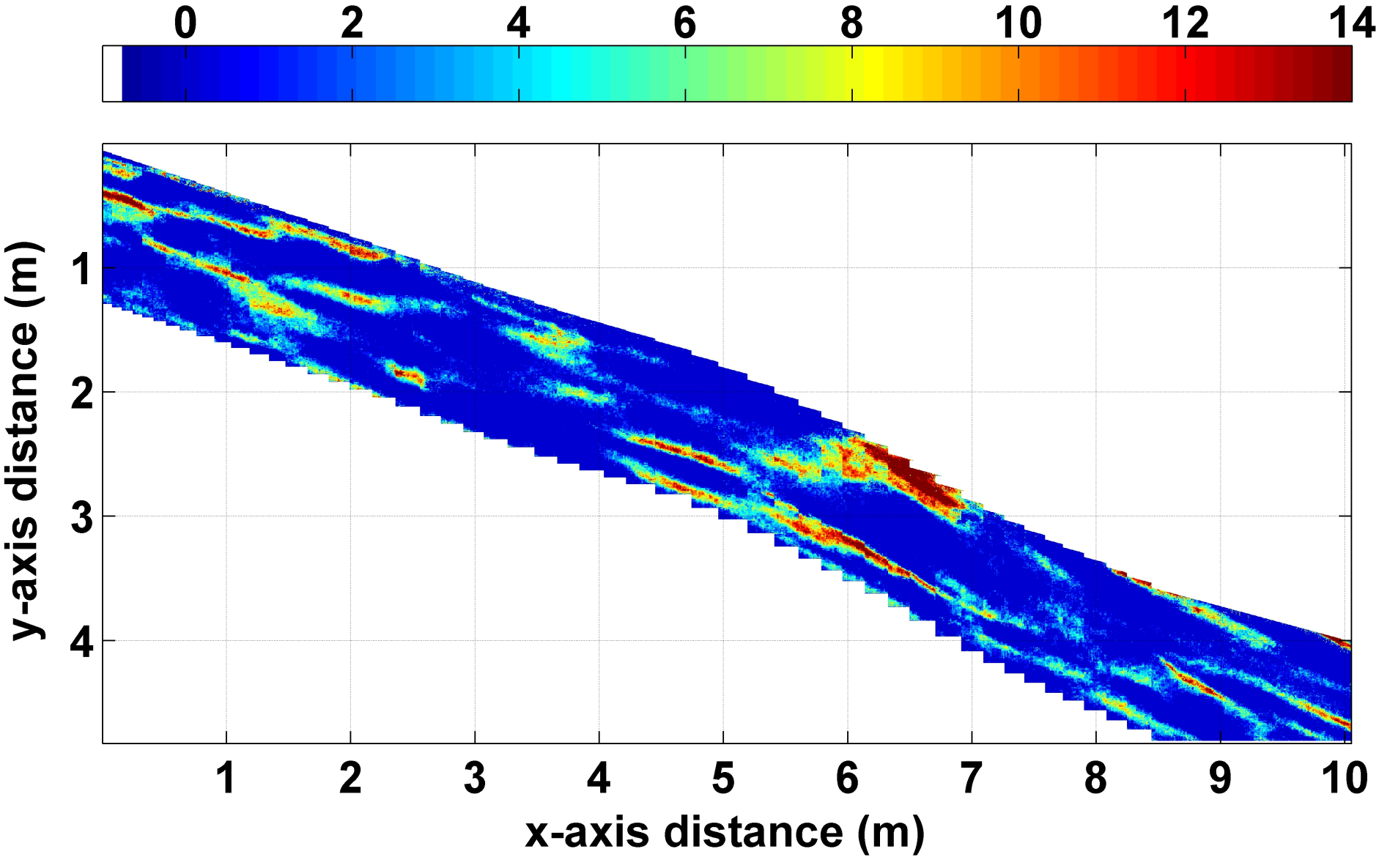
0
2
4
6
8
10
12
14
y-axis distance (m)
1
2
3
4
1
2
3
4
5
6
7
8
9
10
x-axis distance (m)